Marine and Petroleum Geology 143 (2022) 105776

Contents lists available at ScienceDirect

Marine and Petroleum Geology

journal homepage: www.elsevier.com/locate/marpetgeo

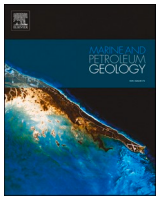

Exploring seismic detection and resolution thresholds of fault zones and gas seeps in the shallow subsurface using seismic modelling

Thea Sveva Faleide [a,b,*], Alvar Braathen [a], Isabelle Lecomte [c], Ingrid Anell [a]

[a] Department of Geosciences, University of Oslo, Box 1047 Blindern, 0316, Oslo, Norway
[b] Norwegian Geotechnical Institute, Box 3930 Ullevål Stadion, 0806, Oslo, Norway
[c] Department of Earth Science, University of Bergen, Box 7803, 5020, Bergen, Norway

ARTICLE INFO

Keywords:
Faults
Seismic imaging and resolution
Seismic modelling
CO_2
Gas seeps

ABSTRACT

Seismic resolution and illumination issues are sources of challenges in the detailed imaging and detection of subsurface fault architecture and fluid migration. Improved constraints on resolution can provide input into monitoring requirements and detectability of CO_2 leakage, and fault-sealing properties during subsurface visualization of migration pathways. This study explores detection and resolution thresholds via synthetic seismic imaging of a detailed shallow normal fault model with realistic fault architecture including sub-seismic structures of damage zones. The base fault model is built from interpretations of high-resolution P-Cable seismic data and is further developed and conditioned by outcrop-based observations and empirical laws for fracture and deformation band distribution. Damage zones of sandstone layers host deformation bands contrary to shale layers with fractures, while mixed lithologies (shaley sandstone and sandy shale) are subjected to a combination of the two deformation mechanisms. We utilize a 2D point-spread function based convolution seismic modelling to produce the synthetic seismic images. Test scenarios include one baseline fault model without a damage zone (M1), and five more advanced/detailed fault models incorporating features known from outcrops (M2-M6; damage zones, an isolated fracture corridor, and gas seeps (CO_2) along damage zones of faults and in the fracture corridor). Furthermore, sensitivity analyses on two selected models test the effect of changing the illumination angle and wavelet. The results show that: (1) faults with damage zones have larger disturbances in seismic signals than faults without damage zones, (2) stronger amplitudes are distinguished for models with CO_2-filled fractures, (3) a fracture corridor (5 m at it widest) is clearly visible where it crosses horizons bounding horizontal layers, (4) sensitivity tests show good imaging for illumination $\geq 45^{\circ}$, which is the average dip of the main fault segment, and (5) learnings from fault modelling offer guidance for seismic monitoring.

1. Introduction

Sedimentary basins host significant geological resources including fossil fuels and potential CO_2 storage sites. For structural traps associated with these, faults are often important features for seal integrity. For CO_2 storage sites in particular, identifying detection and resolution thresholds for gas seeps along faults is of vital importance for site integrity and monitoring.

Fault zones comprise heterogeneous, tabular bodies of rocks that have altered properties compared to the host-rock, from either strain or diagenetic effects. Outcrop studies document faults as narrow, high-strain fault cores with one or several slip surfaces that accumulate most of the throw. The fault core is surrounded by a halo of discrete structures (e.g., fractures and deformation bands) in low-strain damage zones (Fig. 1; Wibberley et al., 2008; Braathen et al., 2009; Childs et al., 2009; Fossen, 2010; Torabi et al., 2020).

Detection and resolution limits in seismic imaging of faults rarely allow identification of this subdivision, although amplitude changes associated with fault zones have been attributed to strained rock volumes (Botter et al., 2014, 2016; Alaei and Torabi, 2017). The limitations in detectability, illumination and resolution cause uncertainties and pitfalls regarding fault geometries (Bond, 2015; Schaaf and Bond, 2019; Michie et al., 2021; Faleide et al., 2021). Such uncertainties are well illustrated by synthetic seismic sections based on simple geological models. To further our understanding of subsurface faults we have to establish and test more realistic models of fault architecture and

* Corresponding author. Department of Geosciences, University of Oslo, Box 1047 Blindern, 0316, Oslo, Norway.
E-mail addresses: t.s.faleide@geo.uio.no, thea.sveva.faleide@ngi.no (T.S. Faleide).

https://doi.org/10.1016/j.marpetgeo.2022.105776
Received 30 September 2021; Received in revised form 31 May 2022; Accepted 1 June 2022
Available online 17 June 2022

properties, including deformation zones.

The fundamental question addressed by this study is: to what degree detailed fault architectures and gas seeps can be detected and resolved in seismic data? As a baseline case, a high-resolution P-Cable dataset (Planke et al., 2009, 2010) from the Hoop area in the SW Barents Sea is used, which hosts a well-imaged fault forming the basis for a fault model guided by the findings of Faleide et al. (2021). It is worth noting that the present study has a generic focus, and is not a case study of the geological evolution of the Hoop area. The baseline model for this study, M1, consists of a fault (F2 from Faleide et al., 2021) that lacks a damage zone. The baseline fault model is further developed into five alternative models (M2-M6) by incorporating features known from outcrops (e.g., Schueller et al., 2013; Ogata et al., 2014). These include a more realistic fault architecture characterized by a damage zone with deformation bands and fractures dependent on varying clastic lithologies as well as the presence of a fracture corridor (Fig. 1).

As an important step towards seismic monitoring of CO_2 storage, we introduce gas/CO_2 in potential reservoirs and along the fault and fracture corridor to see the effects in the seismic imaging. Each model forms the basis for 2D point-spread function (PSF)-based seismic convolution modelling (Lecomte et al., 2015) to systematically explore how seismic reflection data, both high-resolution and conventional, image such structures. The seismic modelling tests detection and resolution thresholds for the observation of various fault architectures and gas seepage along these realistically designed faults and allows for the identification of subtle signature-changes attached to fault architecture and gas saturation.

Furthering our understanding of the ability to image the complexity of fault zones, distribution and composition of the damage zone and identification of potential fluid pathways within them is important for site verification. It is also useful for improving the general understanding of limitations and pitfalls in fault interpretation, thereby potentially contributing to economic de-risking and more sustainable usage of resources.

2. Data and geological setting

The seismic data guiding the fault models are from the eastern flank of the Hoop Fault Complex, offshore in the Barents Sea, more specifically around the Gemini North well (Fig. 2). In this area, Faleide et al. (2021) performed a detailed study of two normal faults (F1 and F2 in Fig. 2c), addressing objective and subjective uncertainties associated with seismic interpretation of faults. In this study, the focus is restricted to fault F2 (Fig. 2c–e).

The baseline model in this study (i.e., a fault without a damage zone, M1), builds on interpretations of fault F2 on a WNW-ESE seismic section in the HR14_3D_HFCE1 high-resolution P-Cable seismic volume (Figs. 2e and 3) by a test panel with different geological backgrounds, as presented and analysed in Faleide et al. (2021). The high-resolution seismic cube overlap with a conventional seismic cube (Fig. 2b). The P-Cable 3D from 2014 (TGS, WGP and VBPR) has a bin size of 4.7 × 6.25 m, whereas the conventional 3D survey from 2012 (TGS) offers a bin size of 12.5 × 18.75 m. Both seismic datasets have zero-phase polarity, and peaks corresponding to an increase in acoustic impedance are represented as red. The dominant frequency is 150 Hz (P-Cable) and 40 Hz (conventional), corresponding to a vertical seismic resolution of about 5 m and 20 m, respectively (Fig. 2d and e).

Stratigraphy and related elastic properties are constrained from well 7325/4–1 (Gemini North; Fig. 4). The gamma ray (GR), photoelectric factor (PEF) and combined density/neutron porosity logs are used for lithology prediction (Figs. 3b and 4). 1D synthetic seismic traces are created based on the sonic and density logs. For the intervals where density log values are missing, a pseudo-density log is estimated based on standard velocity-density relationships. The time/depth relations

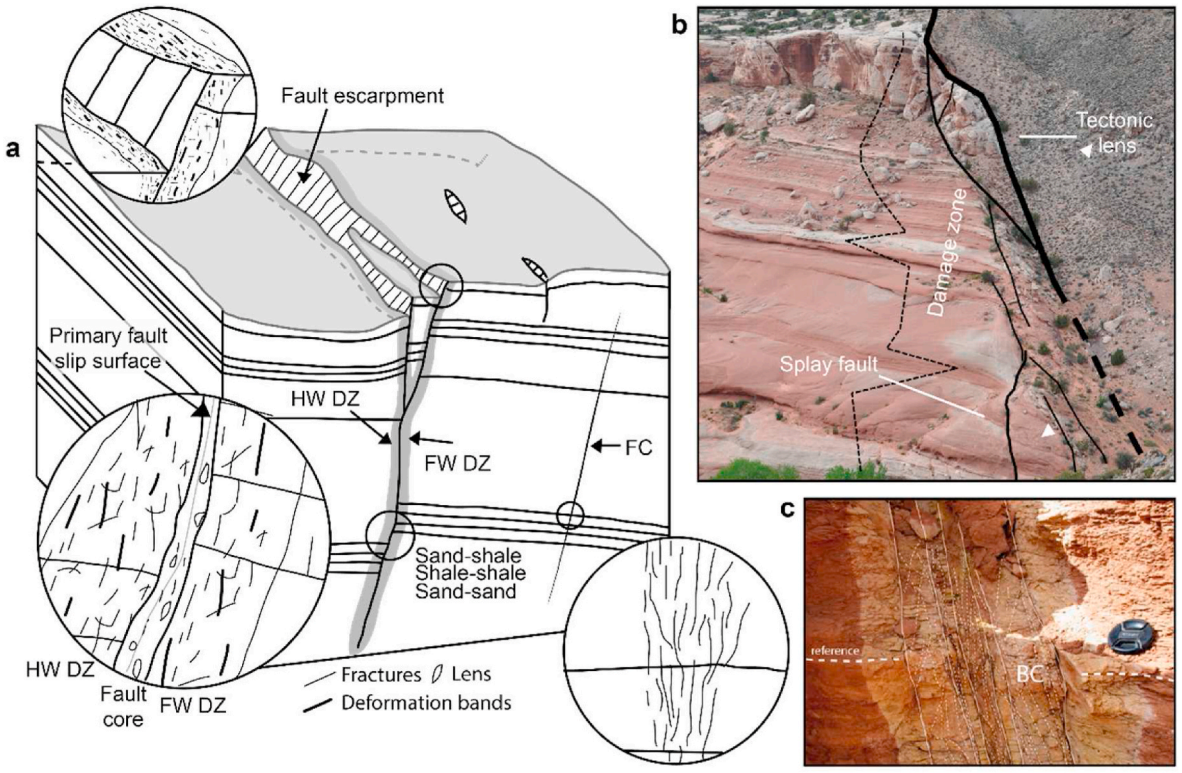

Fig. 1. (a) Schematic 3D fault block showing main elements of fault architecture and an isolated fracture corridor to the right of the main fault. (b) Photograph of the Bartlett Wash Fault (Utah, USA) as an example of outcrop data with a fault core bounded by a wide footwall damage zone in porous sandstones. (c) Example of a fracture corridor in field (Ogata et al., 2014). Figure is modified from Faleide et al. (2021). Abbreviations: BC – bed-confined, DZ – damage zone, FC – Fracture corridor, FW – footwall, HW – hanging wall.

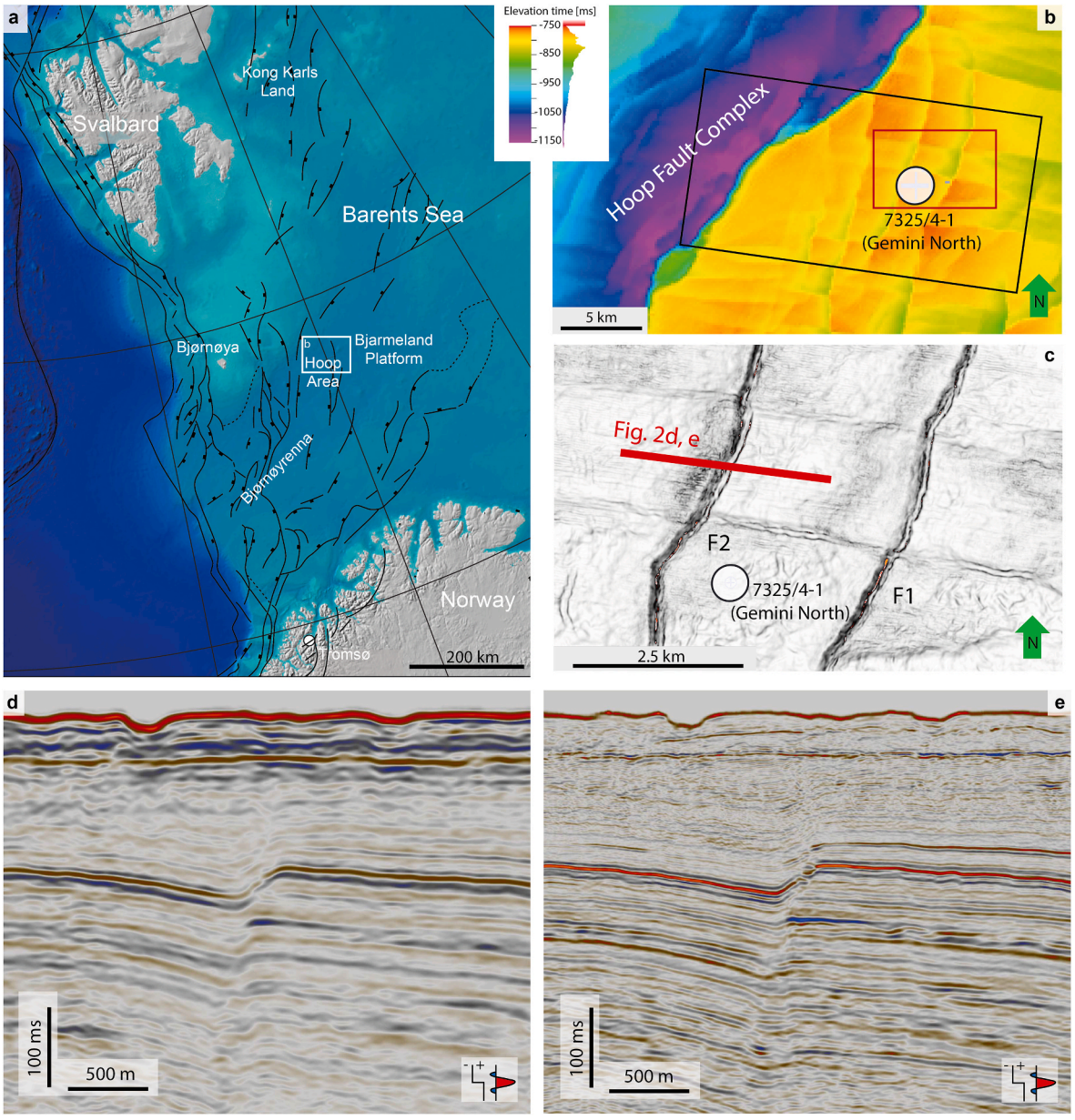

Fig. 2. Regional setting and overview of the study area. (a) Location of the Hoop area in the western Barents Sea midway between Mainland Norway and Svalbard (modified from Faleide et al., 2019). (b) The time-structure map of the Lower Cretaceous Unconformity (LCU) horizon is interpreted in the conventional seismic cube (zoom in of LCU map in Faleide et al., 2021). The outline of the 3D high-resolution seismic cube is marked as a black box, and the Gemini North well is noted. The red box shows the location of c. (c) Variance map in the high-resolution seismic cube (slice at 800 ms depth). Of faults F1 and F2, the latter is focused herein. (d) Uninterpreted conventional WNW-ESE seismic line (arbitrary line coinciding with high-resolution line in e). (e) Uninterpreted high-resolution WNW-ESE seismic line (inline). Location of the seismic lines in d and e is marked in c. Seismic data courtesy of TGS, WGP and VBPR. (For interpretation of the references to colour in this figure legend, the reader is referred to the Web version of this article.)

measured in the well provide seismic velocity information (P-wave velocity, Vp) used for depth conversion (Figs. 3 and 4).

The targeted succession of this study consists of the Middle Triassic to Middle Jurassic Kapp Toscana Group and the Middle Jurassic to Lower Cretaceous Adventdalen Group (Fig. 4; Worsley, 2008). The Kapp Toscana Group, comprising the Snadd, Fruholmen, Tubåen, Nordmela and Stø formations, is dominated by variable mudstones, siltstones and sandstones deposited in pro-deltaic, shallow marine, coastal and fluvial environments (Klausen et al., 2018). The Stø Formation comprises the most mature and well-sorted sandstones of the succession with reservoir-grade deposits occurring in the fine to medium grained cross-bedded sandstones from upper shore-face deposits (Mendoza et al., 2019) and porosity estimates from logs are 20–24% (Farazani, 2017). Shales dominate the overlying Adventdalen Group of Fuglen/Hekkingen to Kolmule formations, which were deposited during a marine highstand cutting off the supply of coarse clastics (Worsley, 2008). Several intervals consist of organic-rich paper shales deposited in deep marine anoxic conditions with high organic productivity. The uppermost deposits comprise the Quaternary above the Upper Regional Unconformity (URU; Fig. 4) that consists of thick prograding wedges of sheet-like clay-silt and sandstone units, transitioning into glaciomarine deposits in the upper parts (Ottesen et al., 2009).

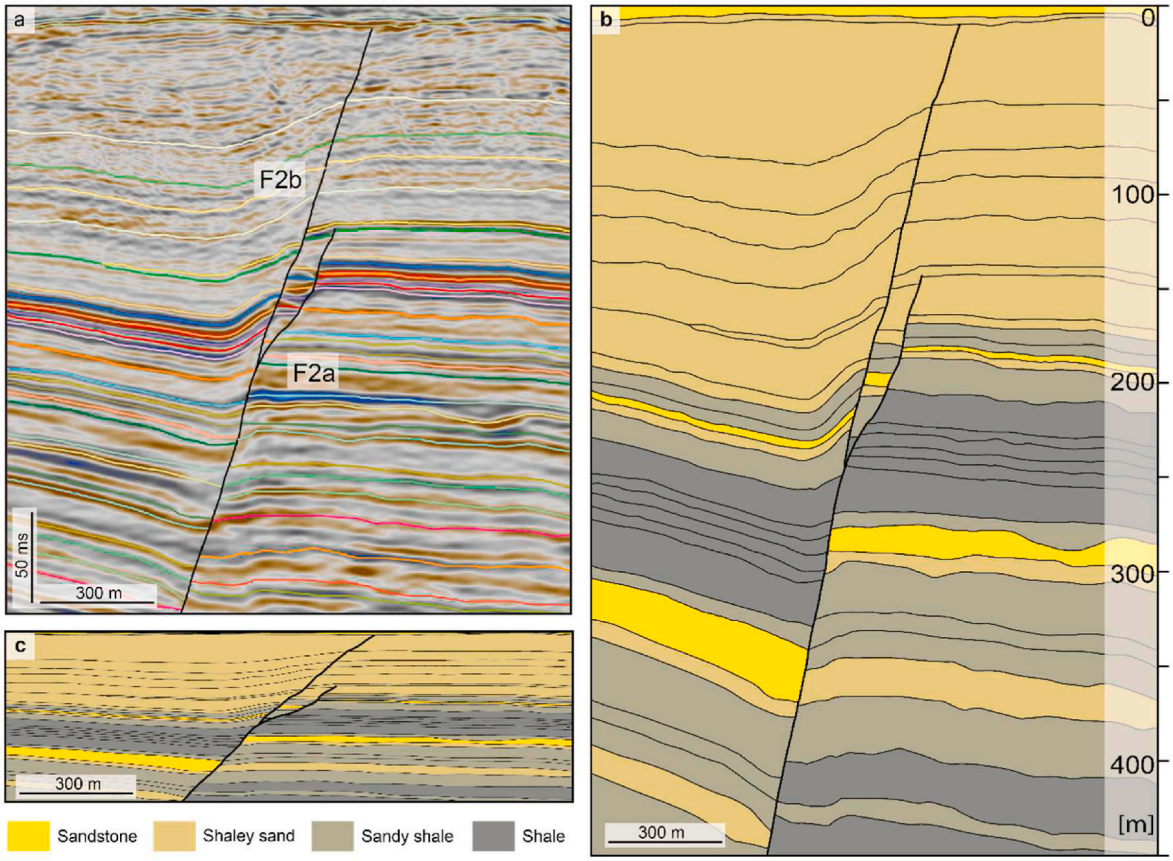

Fig. 3. (a) The fault interpretation and corresponding traced horizons based on scenario 2.4 in Faleide et al. (2021) on top of the high-resolution seismic data (in time). See Fig. 2e for uninterpreted seismic. (b) The geological model of the depth converted fault and horizons from (a), represented here as the baseline model (M1). Vertical exaggeration (VE) 5. (c) The baseline model, M1, in 1:1 scale showing a fault that dips approximately 45°. Seismic data courtesy of TGS, WGP and VBPR.

3. Methods and workflows

3.1. Model building - input to fault and fracture corridor models

The baseline model (Fig. 3) is adopted from Faleide et al. (2021) based on fault interpretation and corresponding traced horizons in high-resolution seismic data belonging to one of their scenarios (2.4) in a study addressing seismic interpretation uncertainties of subsurface faults. In this model the fault is interpreted as a single line in the 2D section. The traced horizons and fault segments are depth-converted according to the two-way travel time (TWT) and average velocity information from the Gemini North well. The depth-converted horizons and faults are exported as an image and imported to a graphics program (in an artboard with a reasonable pixel size relative to the size of the model; preferable 1 px = 1 m, corresponding to 1 m sampling) where they are converted to editable traces. Each layer, 32 in total, is assigned a colour indicative of lithology. Since faults are often represented in seismic data by the displacement of layers/reflections, and not the fault plane itself, fault picks are removed. The resultant model is exported as a PNG file, ready for input to the seismic modelling software.

The stratigraphy is divided into four lithologies; sandstone, shaley sandstone, sandy shale and shale. The boundary between the lithologies is based on the GR log response from the Gemini North well, which covers the whole interval. A sand and shale line are set based on the average values for the layers corresponding to well-known sandstone (Stø Formation) and shale (Fuglen and Hekkingen formations) units (Fig. 4). The sandstone layers in the lower Stø Formation are the reference for clean sand with GR = 70 API and PEF = 2.25 b/electron. The PEF value supports the definition of sand (Mondol, 2015). The sandstone line is set to 75 API, and therefore all layers with GR < 75 is defined as sandstone in this study. The shaley Fuglen Formation is the reference for clean shale, with a high GR response around 160–165 API, along with the fine-grained Hekkingen Formation with values of 130–150 API. Based on these formations the shale line is set to 130 API. The high PEF value of 3.46 b/electron supports the shale definition (Mondol, 2015). Rock units falling between the sand and shale lines of the GR log are divided into two mixed lithologies, i.e., shaley sandstone with a GR response of 75–102 API and sandy shale with a GR response of 102–130 API. The combined Density/Neutron log supports the lithology interpretation (Fig. 4).

The baseline model (M1) is further developed by incorporating structural features known from detailed studies of outcrops in the field. Such studies have established robust statistical relationships between fault throw, fault core thickness and damage zone width and intensity (e.g., Bastesen et al., 2013; Schueller et al., 2013; Choi et al., 2016; Torabi et al., 2020), allowing conditioning of fault zone architecture in modelling (Braathen et al., 2009). Empirical relationships between fault throws and the width of the damage zone, established by Schueller et al. (2013), have been utilized to make a damage zone for the F2 fault (Fig. 5). Their statistical damage zone model is established for highly porous sandstones, but is herein applied to all units irrespective of lithology for simplification. This approach adheres to the conclusion of Torabi et al. (2020) on fault scaling, advocating that damage zones offer similar trends irrespective of lithology and corresponding style of deformation. Further, the width of the damage zone is considered similar for the hanging wall and footwall to the fault.

Damage zones can be further subdivided into inner and outer zones (Fig. 5b and c), from differences in spatial frequency of structures (e.g., Berg and Skar, 2005). As fault core widths are on the cm-dm scale, they are herein, for practical purposes considered parts of the inner damage

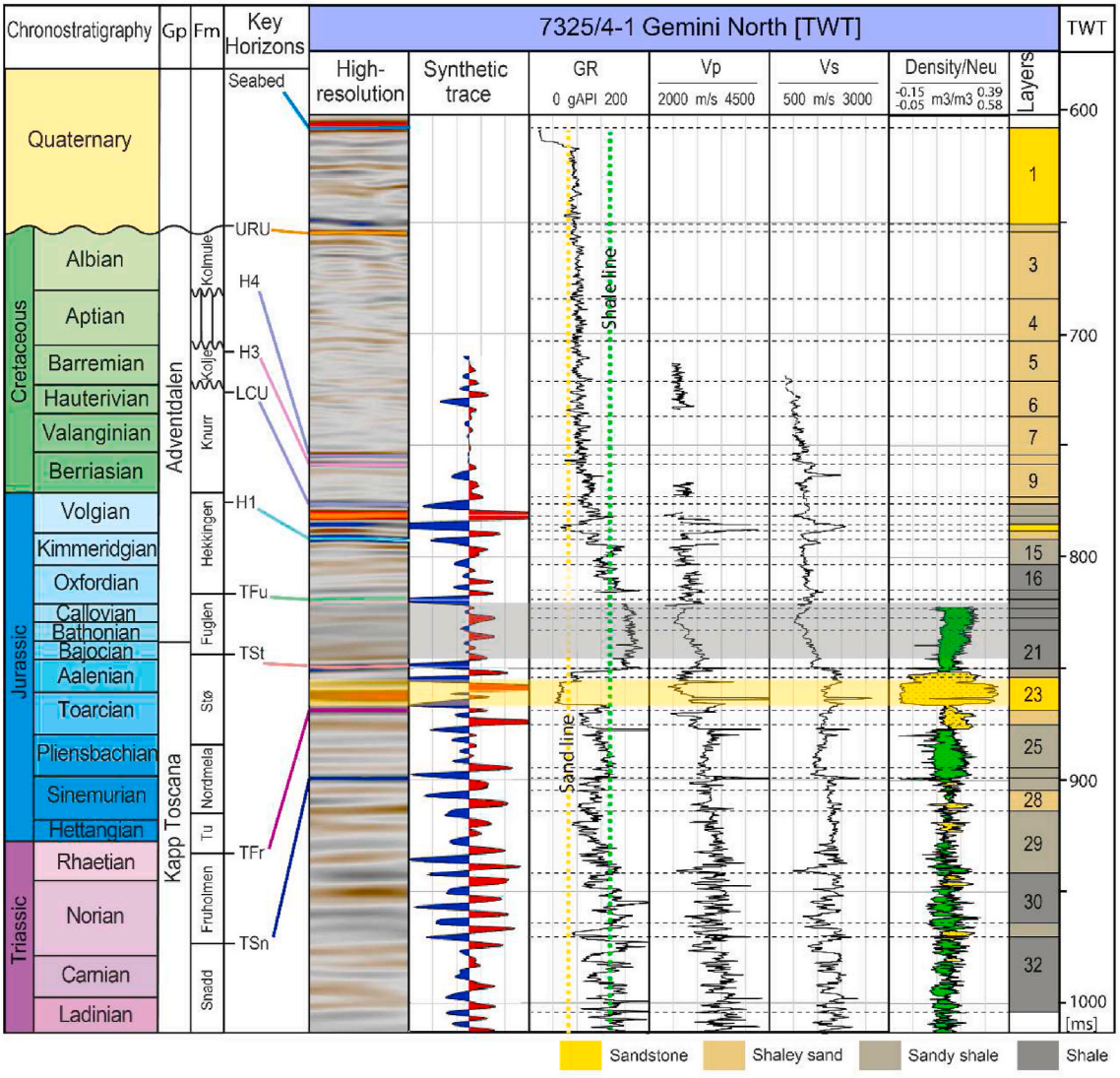

Fig. 4. Seismic stratigraphic and chronostratigraphic framework of the Upper Triassic, Jurassic and Lower Cretaceous succession in the Hoop area at the Gemini North well (7325/4–1). Modified from Faleide et al. (2021). The seismic stratigraphic framework for the Lower Cretaceous is based on, and updated from, the study of Faleide et al. (2019), while the Jurassic and Triassic framework is based on given depths of the formation tops in the Gemini North well from the Norwegian Petroleum Directorate FactPages (https://factpages.npd.no/). The chronostratigraphic panel is modified from Cohen et al. (2013). The well panel includes the seismic data, modelled synthetic traces for the high-resolution data, gamma ray (GR), P-wave velocity (Vp), S-wave velocity (Vs), density/neutron plot and the layers colored with respect to its lithology (same colour legend as in Fig. 3). The horizons bounding the layers are marked on the well data (stippled black lines), while the formation tops are marked/correlated for the corresponding reflections in the seismic data. The picked shale and sandstone lines are marked on the GR well log. The main sandstone and shale units that were used for lithology classification based on the GR log are outlined in yellow and grey respectively. Abbreviations: URU – Upper Regional Unconformity, LCU – Lower Cretaceous Unconformity, Fm – Formation, Gp – Group, Tu – Tubåen, TWT – two-way travel time, ms – millisecond, H – Horizon, TFu – Top Fuglen, TSt – Top Stø, TFr – Top Fruholmen, TSn – Top Snadd. Seismic data courtesy of TGS, WGP and VBPR. (For interpretation of the references to colour in this figure legend, the reader is referred to the Web version of this article.)

zone. The width of the fault damage zone, with subdivision into inner and outer, is determined based on fault throw, which has a maximum of about 60 m but varies along the F2 fault (Fig. 5b). The corresponding maximum width of the damage zone is about 50 m. Throw is calculated for each stratigraphic unit (Fig. 5b), guiding damage zone width and subdivisions of structural element intensity as described in Schueller et al. (2013):

$$W1av = 3.67T^{0.46} \quad (1)$$

$$W5av = 2.32T^{0.46} \quad (2)$$

$$W10av = 1.41T^{0.44} \quad (3)$$

where T = throw in m and Wx = width in m from the fault core. The x value of 1, 5 or 10 represents the deformation band density reached at the distance Wx from the fault core, either in the footwall or in the hanging wall (Schueller et al., 2013). Inner damage zones are represented by the W10 zone = W10av (Eq. (3)), whereas outer damage zones are represented by the W1 zone = W1av (Eq. (1)) – W10av (Eq. (3)). As the W5 zone (W5av (Eq. (2))) appears narrow in field observations (e.g., the Bartlet Wash Fault; Fig. 1b), this zone has been omitted.

Fracture corridors, as outlined in Ogata et al. (2014) and Gabrielsen and Braathen (2014), appear as damage zones along faults and around fault-tips, thereby corresponding with fault zone strain outlined above. In two models (M5 and M6), one isolated fracture corridor caused by fold-crest dilation or fault-tip process zone, without shear offset of markers (Ogata et al., 2014), is included (Fig. 5). Joints are implemented

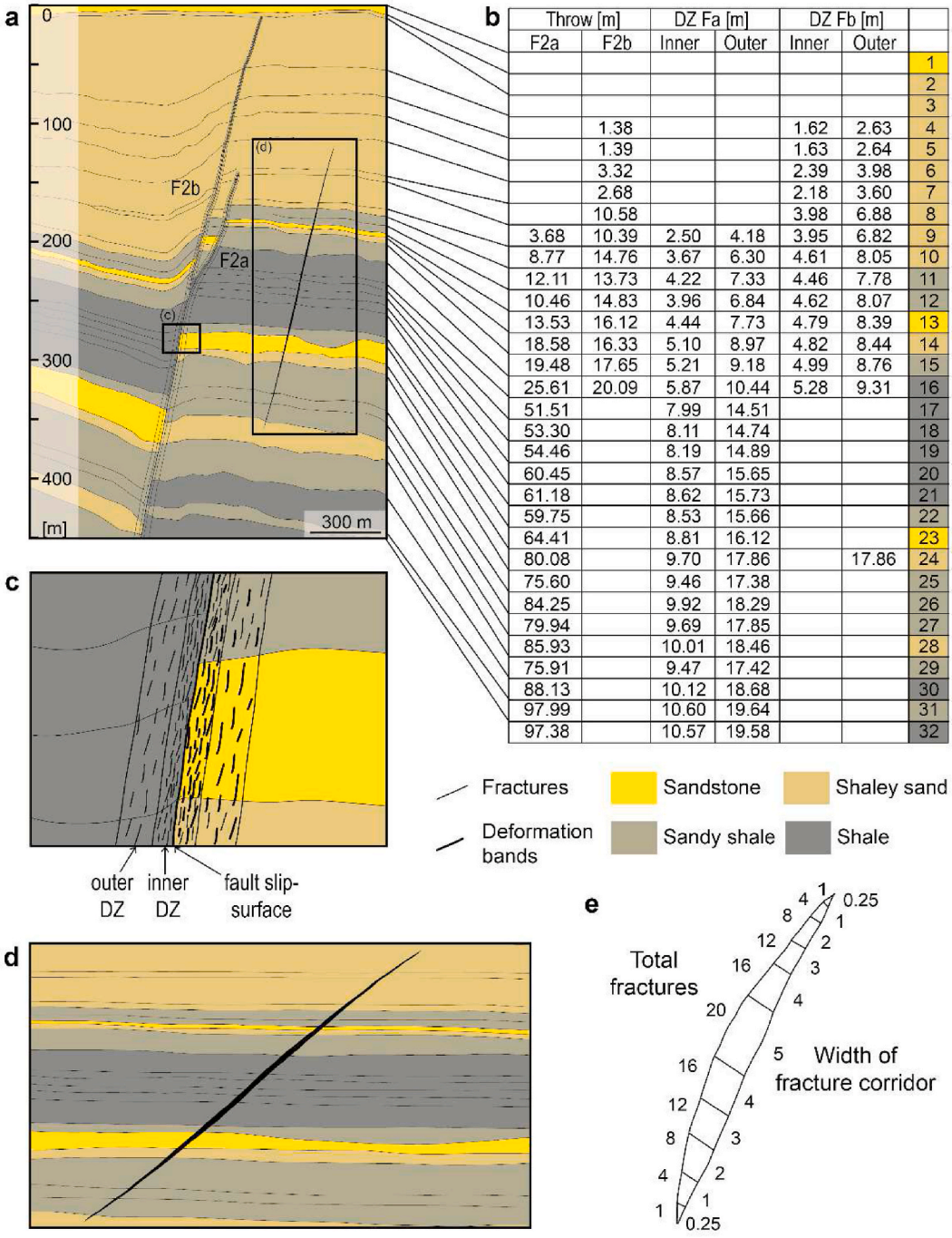

Throw [m]		DZ Fa [m]		DZ Fb [m]		
F2a	F2b	Inner	Outer	Inner	Outer	
						1
						2
						3
	1.38			1.62	2.63	4
	1.39			1.63	2.64	5
	3.32			2.39	3.98	6
	2.68			2.18	3.60	7
	10.58			3.98	6.88	8
3.68	10.39	2.50	4.18	3.95	6.82	9
8.77	14.76	3.67	6.30	4.61	8.05	10
12.11	13.73	4.22	7.33	4.46	7.78	11
10.46	14.83	3.96	6.84	4.62	8.07	12
13.53	16.12	4.44	7.73	4.79	8.39	13
18.58	16.33	5.10	8.97	4.82	8.44	14
19.48	17.65	5.21	9.18	4.99	8.76	15
25.61	20.09	5.87	10.44	5.28	9.31	16
51.51		7.99	14.51			17
53.30		8.11	14.74			18
54.46		8.19	14.89			19
60.45		8.57	15.65			20
61.18		8.62	15.73			21
59.75		8.53	15.66			22
64.41		8.81	16.12			23
80.08		9.70	17.86		17.86	24
75.60		9.46	17.38			25
84.25		9.92	18.29			26
79.94		9.69	17.85			27
85.93		10.01	18.46			28
75.91		9.47	17.42			29
88.13		10.12	18.68			30
97.99		10.60	19.64			31
97.38		10.57	19.58			32

Fig. 5. The main parameters used for building the geological models. (a) The geological model shown is M5 (vertical exaggeration, VE, of 5). The stratigraphy (32 layers) is divided into four lithologies: sandstone, shaley sand, sandy shale and shale. (b) The damage zone (inner and outer) for the fault is included based on empirical relationships between fault throws and the width of the damage zone, established by Schueller et al. (2013). (c) Zoom in of the geological model (VE 5) in a, and with the addition of fractures/deformation bands. (d) Zoom in around the isolated fracture corridor of the geological model in a (1:1 scale). (e) Detailed conceptual outline of the fracture corridor with the width and total number of fractures (based on Ogata et al., 2014). Abbreviations: DZ – Damage Zone.

structures that are distributed as 20 joints (4 joints/meter) at the maximum width of 5 m, trailing off towards the tips, as shown in Fig. 5d and e.

3.2. Conditioning elastic properties of lithologies and rock damage

With implementation of fault damage, elastic parameters (Vp, Vs, density) vary in layers within the damage zone close to the fault (Fig. 5; Table 1). Fault strain in clean sandstone is conditioned as deformation bands, whereas shale units host fractures. For mixed, interlayered lithologies, both deformation bands and fractures are applied. Rock properties are influenced by rock strain (dilation or compaction; e.g., Braathen et al., 2020), partly guided by host-rock porosity. High-porosity sandy layers (>12–15% porosity) deform by deformation bands, envisioned as cataclastic shear-compaction bands herein (e.g., Fossen et al., 2007, 2018). Damage zone compaction causes a decrease in porosity and a corresponding increase in velocity and density. For lower-porosity units (<15%), such as shales, the damage zone is dominated by fractures. Contrary to deformation bands, fractures dilate rocks, thereby increasing porosity with corresponding decreases in

Table 1
How the elastic parameters change from the undamaged rock to the deformed rock in the inner and outer damage zones, and when CO_2 is present in the damage zone. Values taken from Botter (PhD thesis) based on Sigernes (PhD thesis). The new Vp, Vs and density are presented in Table A1 in Appendix A. *Density is calculated with Gardners relation (Appendix A) based on the new estimated Vp.

	Inner damage zone			Outer damage zone			Damage zone with CO2		
Lithology:	Vp	Vs	ρ	Vp	Vs	ρ	Vp	Vs	ρ
Sand	1.3	1.3	*	1.15	1.15	*	1.0	1.0	*
Shaley sand	1.1	1.1	*	1.05	1.05	*	0.87	0.99	*
Sandy shale	0.8	0.9	*	0.9	0.95	*	0.87	0.99	*
Shale	0.6	0.7	*	0.8	0.85	*	0.87	0.99	*

velocity and density (e.g., Sigernes, 2004; Botter, 2016). Furthermore, fluids in fractures impact elastic properties. For instance, when CO_2 in gas phase replaces water in the fractures, there will be an additional decrease in Vp (Agofack et al., 2018). In cases of shaley sandstone, deformation is distributed as 2/3 deformation bands and 1/3 fractures, compared to sandy shale with 1/3 deformation bands and 2/3 fractures.

Based on the Gemini North well (Fig. 4), average parameter values for each of the 32 layers are calculated (Table A1 in Appendix A). The Vp is determined based on the check-shot time-depth information (Fig. 4). For layers that are not covered by the Vs and density log data, the parameters are calculated based on the interval Vp and Vp/Vs ratio for the same typical lithology in the model, and the Gardner's rule (Gardner et al., 1974) relating velocity (Vp; m/s) and density (ρ; g/cm^3), respectively:

$$\rho = 0.31 * V_p^{\frac{1}{4}} \quad (4)$$

In the damage zones, the elastic parameters are adjusted dependant on deformation by fractures or deformation bands, and the distribution of damage (inner and outer damage zone; Table 1 and Table A1 in Appendix A). The effects of deformation are estimated based on values (percentage interval) for maximum decrease and increase of velocity for siliciclastic rocks, based on Botter (2016), Botter et al. (2014, 2016) and references therein. In the models, deformation bands in sandstones cause a 30% increase in Vp and Vs for the inner damage zone and 15% for the outer damage zone. In lower-porosity units with fractures, the predicted decrease in seismic velocity is 40% for Vp and 30% for Vs in the inner damage zone, while Vp and Vs decrease in the outer damage zone by 20% and 15%, respectively. In mixed lithologies (shaley sandstone and sandy shale), the effects between the two end-member type lithologies are scaled. In shaley sandstone, there is a 10% increase for Vp and Vs for the inner damage zone, and a 5% increase for the outer damage zone. For sandy shale, there is a 20% decrease for Vp and a 10% decrease for Vs in the inner damage zone, while Vp and Vs decrease in the outer damage zone by 10% and 5%, respectively. New densities are calculated with Gardner's rule (Eq. (4)) using the new estimated Vp. The values for Vp, Vs and density are presented in Table A1 in Appendix A.

If gaseous CO_2 (or other gases) migrates along a shallow fault, as expected above c. 800 m depth, with gas replacing water in the fractures, Vp will decrease. An additional ~13% reduction of Vp and ~1% reduction of Vs were thus included in the models based on Agofack et al. (2018). These values (Table 1) were used to adjust the elastic parameters both in the inner and outer damage zones for all layers assumed to have fractures filled with gaseous CO_2.

The fracture corridor is divided into 6 intervals (Fig. 5d,e), and the reduction of Vp and Vs is in the range of 40%–2% and 30%–2%, respectively, taken the maximum reduction from the inner damage zone for the shale and interpolating to zero-reduction (outside the fracture corridor; Table 2). Average Vp and Vs from the shale units are used as a basis for the estimation of reduced Vp, Vs and density within the fracture corridor (Table 2).

3.3. Seismic modelling

The main steps of the workflow for the 2D PSF-based seismic convolution modelling (Lecomte et al., 2015, 2016) are presented in Fig. 6 and are similar to Faleide et al. (2021). 2D geological models were first created from depth-converted horizons and fault interpretations (Fig. 6a–c). The models are 1500 m wide and 450 m high, and the sampling interval is 1 m horizontally and 0.2 m vertically. Each layer of the model was then assigned constant elastic parameters (i.e., Vp, Vs and density; Table A1 in Appendix 1) to further calculate the reflectivity using the Zoeppritz equations (Shuey, 1985, Fig. 6d). Given the lack of detailed survey information and a velocity model for the considered data, a simplified and idealized version of the PSF-based convolution modelling is used by directly designing PSFs from a few key parameters (Lecomte et al., 2016). A generic illumination pattern is thus selected, defined by a regular illumination of all reflector dips until a selected maximum (e.g., 0°–45° dip range), in addition to an average velocity, an incident angle, and wavelet extracted from the seismic data. Together these are used to generate a so-called PSDM filter (Fig. 6). The PSF is obtained from a Fourier Transform (FT) of that PSDM filter (Fig. 6e) and convolved with the reflectivity model to obtain a synthetic (PSDM-like) seismic image (Lecomte et al., 2015, 2016). The synthetic seismic image (Fig. 6f) corresponding to the input geological model can then be analysed as a function of various wavelets and the other parameters mentioned above.

In addition, noise is added to the synthetic seismic sections to make it more realistic. The colored-noise model is generated by convolution of a random white reflectivity model with the same PSF used for the synthetic seismic described earlier, thus reproducing the same (PSDM-like) filtering effect that the geological models receive in the seismic modelling. The reflectivity range of the noise model was scaled according to the reflectivity range of the input geological model to test different signal-to-noise ratios. All synthetic seismic sections, including the noise components, were also amplitude-calibrated so that an input – single – horizontal reflector of strength +1 yields a flat reflection with a peak of amplitude +1. With actual data, such amplitude calibration is performed via wavelet estimation for well ties, this to compensate for non-preserved amplitudes due to seismic acquisition, processing and imaging. With the modelling method used here, the seismic amplitudes are constrained from the PSF, which stems itself both from geophysical parameters (e.g., wavelet, incident angle, illumination pattern, etc.; Lecomte, 2008) and from FFT parameters (size and sampling of the imaged area). The single, unit and horizontal reflector test thus allows to compensate for both effects by a simple normalization. This amplitude

Table 2
How the elastic parameters change within the fracture corridor. The density is calculated with Gardners relation (Appendix A) based on the new estimated Vp.

Width [m]	Total Fractures	Reduction Vp	Reduction Vs	Estimated Vp [km/s]	Estimated Vs [km/s]	Estimated density [g/cm^3]
0,25	1	0.98	0.98	2.698	1.247	2.23
1	4	0.90	0.90	2.478	1.145	2.19
2	8	0.80	0.85	2.202	1.082	2.12
3	12	0.70	0.80	1.927	1.018	2.05
4	16	0.65	0.75	1.789	0.954	2.02
5	20	0.60	0.70	1.652	0.891	1.98

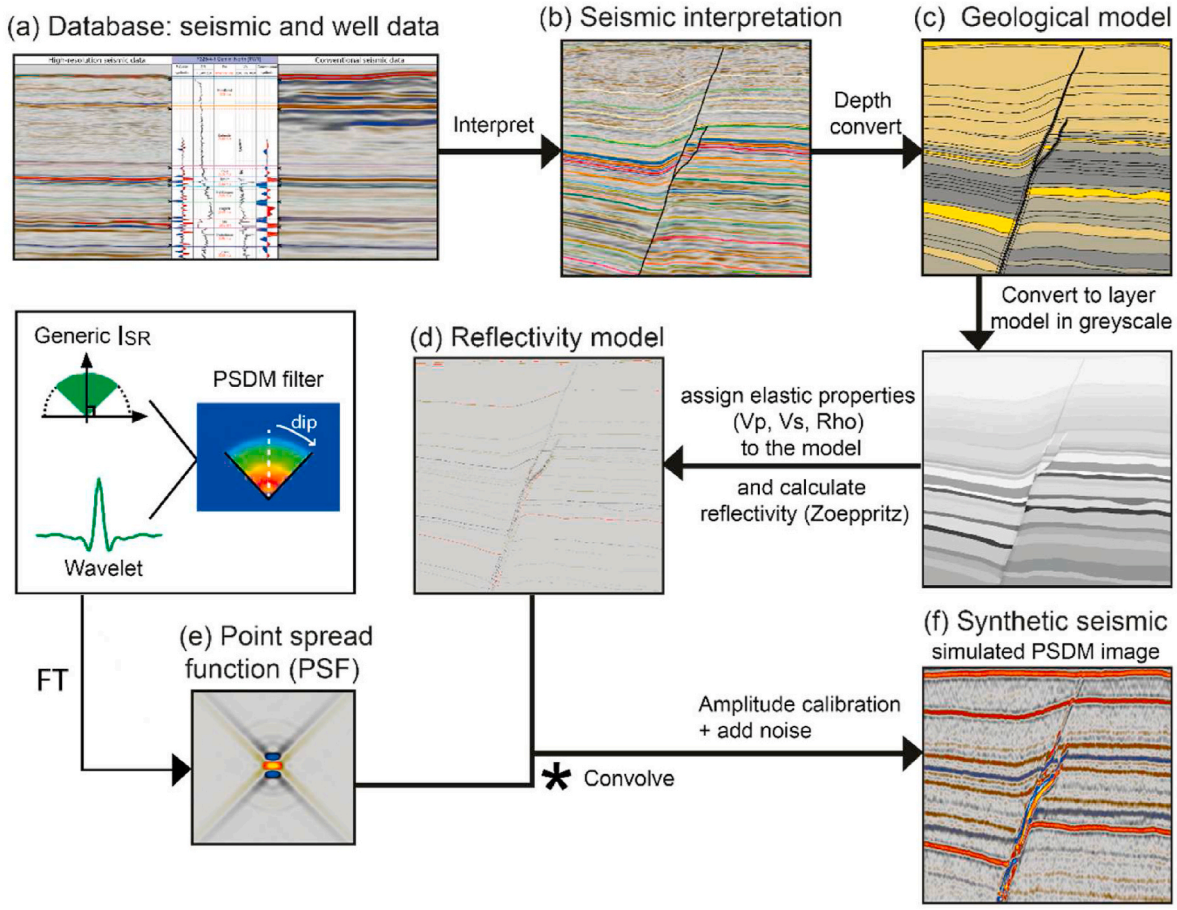

Fig. 6. The main steps of the 2D point-spread function (PSF)-based seismic convolution modelling workflow (figure updated from Faleide et al., 2021). The database (a) consists of post-stack 3D seismic in time and well data. The first step involves the interpretation of the seismic data (b). A geological layered model (c) is created based on depth-converted fault and horizon interpretations. Each layer is assigned constant elastic parameters (i.e., Vp, Vs and density (Rho)), to further calculate the reflectivity (d). The reflectivity model is convolved with a point spread function (PSF) (e) and the output of the seismic modelling is the synthetic seismic image (f). See text for details. Abbreviations: PSDM –Prestack Depth Migration, I_{SR} – Illumination vectors, FT - Fourier Transform. Seismic data courtesy of TGS, WGP and VBPR.

calibration allows therefore direct comparisons between input reflectivity and seismic amplitudes (using the same absolute scales for display), the latter resulting, however, from various interferences (constructive and destructive) of the seismic signals after (PSDM) migration, including the possible lack of illumination of steep reflectors.

A powerful tool for comparison and detection of differences in synthetic seismic sections is to make difference plots. Such difference plots help to emphasize changes between gas-filled vs water-filled damage zones and fracture corridors. Another powerful tool is to compare reflectivity and corresponding synthetic wiggle traces for each model, to see if these match or miss-match, and superimpose seismic wiggle traces for two models together to see the difference in response.

As shown in Table 3, geophysical parameters such as wavelet, incident angle and illumination pattern are varied to, e.g., represent either the conventional or the high-resolution seismic volumes. The wavelets are extracted from the two seismic data types. For the target area around fault F2 (750–850 TWT interval), the dominant frequencies are 40–45 Hz and 90 Hz, respectively (power spectrum in Faleide et al., 2021). The wavelet corresponding to the high-resolution seismic data is mainly used to generate the synthetic seismic images of all geological models. The incident angle for the long-offset conventional seismic data is set to 20°, and for short-offset high-resolution data 0°. The standard geophysical parameters (Table 3) for all models in this study comprise: a 45° illumination angle, implying that reflectors dipping between 0 and 45° will be illuminated; 0° incident angle representing the short-offset high-resolution seismic data, and the wavelet with frequency of 90 Hz. Two of the models, M2 and M5, are tested with both wavelets and different incident angles (0° and 20°) to illustrate the resolution differences between high-resolution and conventional data. Model M2 is also generated/tested with different illumination angles: 30°, 45° (as the standard parameter for all models) and 90° (perfect illumination).

Table 3
Geophysical parameters used for generating the synthetic seismic sections.

Geophysical parameters	M1	M2	M3	M4	M5	M6
45° illumination, 0° incident, P-Cable wavelet,	X	X	X	X	X	X
45° illumination, 20° incident, Conventional wavelet		X			X	
30° illumination, 0° incident, P-Cable wavelet		X				
90° (perfect) illumination, 0° incident, P-Cable wavelet		X				

4. Results of seismic modelling

In total, six geological models (M1-M6) are tested with seismic modelling targeting fault F2 (Figs. 2c, 3a and 7). The models are 1500 m wide, 450 m high and consist of 32 layers (Figs. 3 and 5). The main fault and horizon/layer interpretations are similar in all scenarios, and the widths of the inner and outer damage zone are identical for models M2-

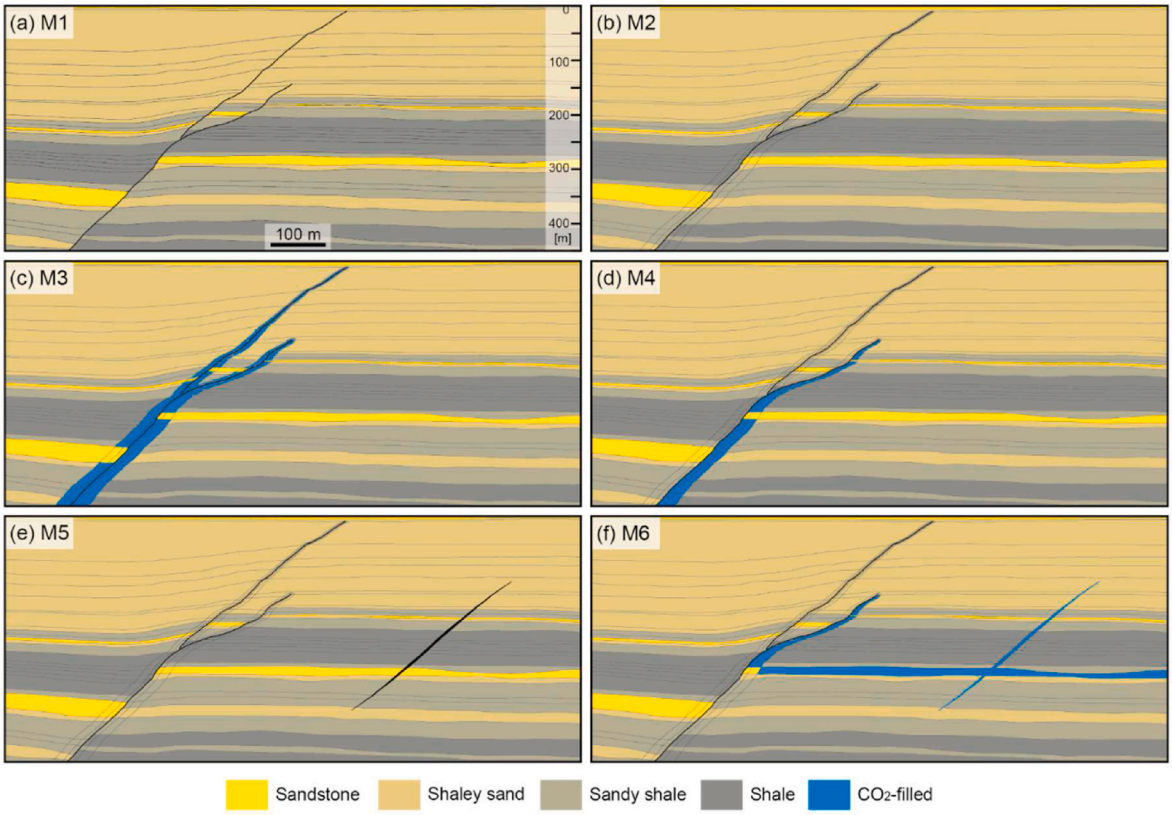

Fig. 7. The six geological fault models presented in 1:1 scale. (a) The baseline geological fault model, M1, without a damage zone. (b) Geological fault model, M2, fault with damage zone. (c) Geological fault model, M3, with CO_2 in both hanging wall and footwall damage zone. (d) Geological fault model, M4, with CO_2 in the F2a footwall damage zone. (e) Geological fault model, M5, with damage zone and an isolated fracture corridor away from the fault. (d) Geological fault model, M6, with CO_2 in the thick sandstone layer 23 and the damage zone above in the F2a footwall and in the fracture corridor. Note that the geometry of the damage zone is the same for models M2-M6 – based on the details documented in Fig. 5.

M6. F2 bifurcates into two segments (F2a, F2b; Figs. 3a and 5a) at around 240 m depth; below this, the fault has a dip of 45°. The two segments above, F2a and F2b, have dips of 25–35° and 40–45°, respectively. F2a terminates within layer 8 whereas F2b extends to the top of the model. Model M1 (the baseline model; based on Faleide et al., 2021) is F2 without a damage zone (Figs. 3b and 7a); model M2 is F2 with damage zone (Fig. 7b); model M3 is F2 with damage zone and CO_2 gas in the footwall and hanging wall (Fig. 7c); model M4 is F2 with damage zone and CO_2 gas in the footwall (Fig. 7d); model M5 is F2 with damage zone and an isolated fracture corridor away from F2 (Figs. 5 and 7e); and model M6 is F2 with damage zone and CO_2 leaking from a sandy reservoir up into the F2a footwall and in the fracture corridor (Fig. 7f). The elastic parameters vary in the layers within the damage zone close to the fault, and within the fracture corridor for the last two models (Tables 1–2 and Table A1 in Appendix A).

4.1. *Synthetic seismic sections of the fault models*

In the high-resolution synthetic seismic section of model M1 (F2 without damage zone; Figs. 3, 7a and 8a), splaying of the F2-fault into segments F2a and F2b is clearly detectable. Internal layers in the fault block, between F2a and F2b, are also well imaged. According to the geological input model (Figs. 3b and 7a), F2a terminates within layer 8 and F2b penetrates up to URU at the base of layer 2 (Fig. 5). The fault tip of F2a is identified in the synthetic seismic section (#1, Fig. 8a), while the upper fault tip of F2b cannot be identified, thereby deviating from the geological model (#2). F2a is imaged below the fault block (#3), just before F2a and F2b merge. In the high-amplitude peak (red) in the deeper part, the fault plane itself is imaged, in what appears as a dragged reflective layer along the fault (#4).

In model M2 (F2 with damage zone; Fig. 7b), the fault is well imaged and both segments F2a and F2b are associated with strong reflections. The termination of F2b around layer 2 and where F2a tips within layer 8, are clearly seen (#5 and #6, Fig. 8b). Overall, there are more disturbances in the fault block between the two segments than outside this block. A smear of the lower boundaries of layers 10 and 14 from the faulted block, across F2b, can be detected in the synthetic seismic section of M2 (#7, Fig. 8b). Furthermore, parts of F2a below branch-point to F2b show enhanced reflections corresponding to the fault envelope having the widest damage zone (50 m). Near the branch-point, especially in the footwall of F2a, the amplitude is stronger, ascribed to overlapping, and hence, wider damage zones (#8, Fig. 8b). This is the case for models M2-M6, all consisting of an inner and outer damage zone (Fig. 7). The fault plane is imaged as dipping reflection along the entire fault.

In model M3 (Fig. 7c), gaseous CO_2 fills all fractures in the hanging wall and footwall damage zones. The synthetic seismic section for this model (Fig. 8c) shows that the fault block between F2a and F2b remains discernible. There are weak reflections between the layers 8 and 10, but there is still an offset in top of layer 8 (#9, Fig. 8c). The layers and zones that are filled with gaseous CO_2 appear brighter in the synthetic seismic sections (#8, Fig. 8c).

Model M4 deviates from M3 in that CO_2 is only filling the damage zone in the footwall of F2a (Fig. 7d). The synthetic seismic section of M4 (Fig. 8d) mimics that of M3 (Fig. 8c), clearly showing the termination of both F2a and F2b, and a strong amplitude in the F2a footwall (at #8).

In model M5, an isolated fracture corridor has been added to M2 east of F2 (Figs. 5a and 7e). This fracture corridor is well imaged in the synthetic seismic section, as a dipping signal modification, imaged as two to three dipping reflections (#10 in Fig. 9c) cutting the horizontal

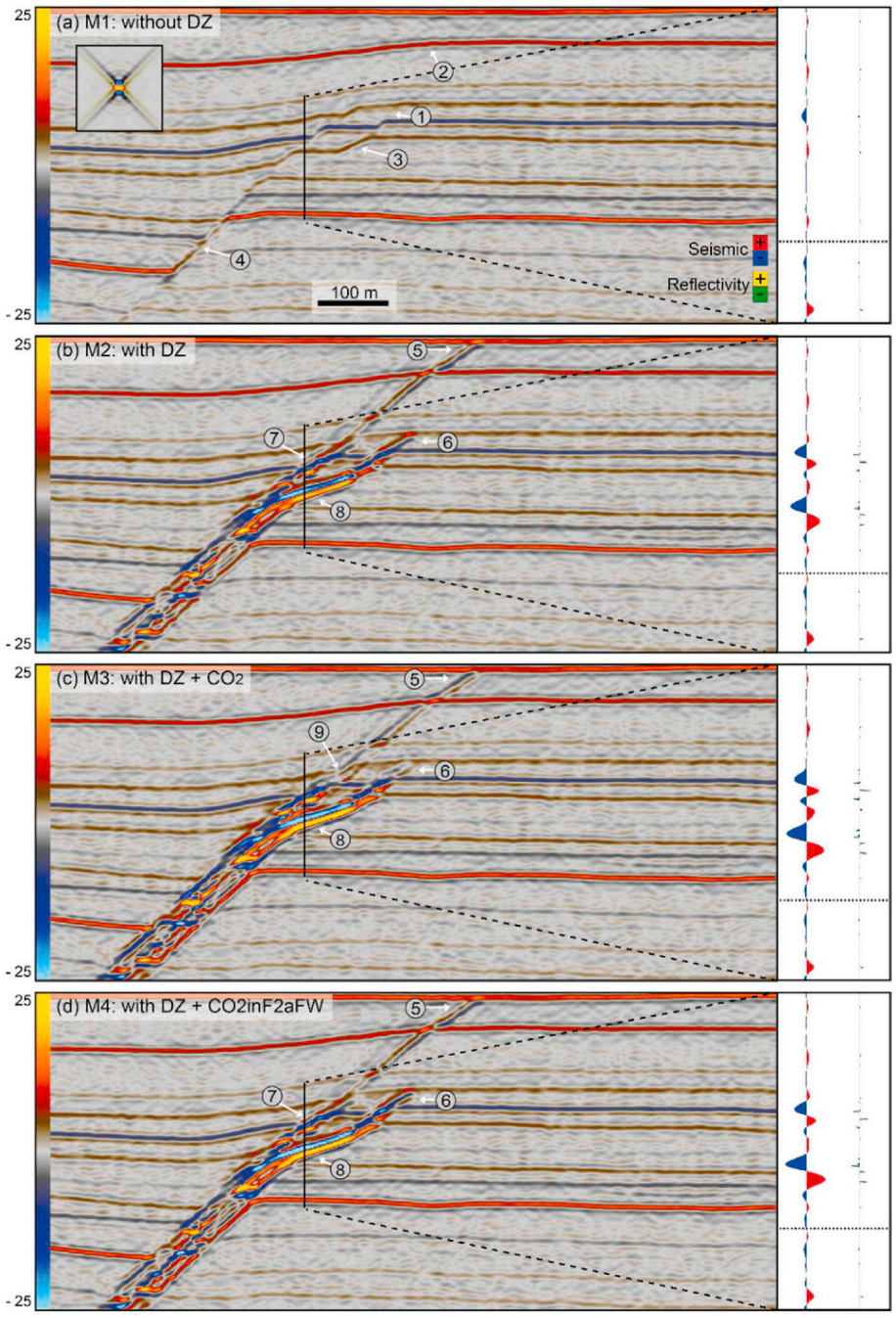

Fig. 8. Synthetic seismic sections for models M1-M4. The following standard seismic modelling parameters are utilized: Illumination angle (45°), wavelet corresponding to high-resolution data, incident angle (0°), average velocity (2,72 km/s). Noise is added to the synthetic seismic. (a) Synthetic seismic section of the baseline model (M1), without damage zone (DZ). The PSF and scale (1:1) are the same for all synthetic seismic profiles. (b) Synthetic seismic section of M2: with damage zone; (c) M3: with damage zone and CO_2-filled fractures in both hanging wall and footwall of F2 (F2a and F2b); and (d) M4: with damage zone and CO_2-filled fractures in the footwall of F2a. The numbered labels point out key observations described in the text. The geological models for M1-M4 are presented in Fig. 7a–d. The reflectivity (reflection coefficients) and corresponding synthetic wiggle trace for the interval marked with a vertical line shown for each model. Where the CO_2 is present, the amplitude is stronger.

layers. In accordance with the geological model, there is no sign of stratigraphic offset.

Model M6 presents a fault model with damage zone and a fracture corridor similar to M5. In addition, gaseous CO_2 is present in the undamaged thickest sandstone layer in the deep parts and with envisioned leaks to the fractures in the F2a footwall damage zone and the fracture corridor (Fig. 7f). The blue reflections (trough) reflect very strong amplitudes in the footwall compared to the hanging wall. In the hanging wall, the same interval appears as two bright reflections with no reflections between them (#11, Fig. 9d). A depression to the right of the fracture corridor in the geological model (Fig. 7e and f), the sandy shale above the deepest and thickest sandstone layer, can be seen as an isolated depression (channel?) in the synthetic seismic section (#12 in Fig. 9b,d).

4.2. Comparison of synthetic seismic sections

In the synthetic seismic sections for the fault models with damage zone (models M2-M6), the upper part of F2b is better imaged compared to the model without damage zone (M1) for which F2b does not cut layers 3 and 4 (Figs. 8 and 9). The damage zone and the fracture corridor of fault models M2-M6 appear wider in imaged synthetic seismic sections (Figs. 8 and 9) compared to the geological models (Fig. 7). The synthetic seismic results show that the fault appears better imaged in all cases when damage zones are added, mainly driven by stronger amplitudes (#8, Figs. 8 and 9).

CO_2-filled fractures create stronger (high-amplitude) reflections (models M3, M4 and M6; Figs. 8 and 9) as the change in elastic parameters results in larger changes in velocity and density from the undamaged rock to the deformed rock in the damage zones. The model

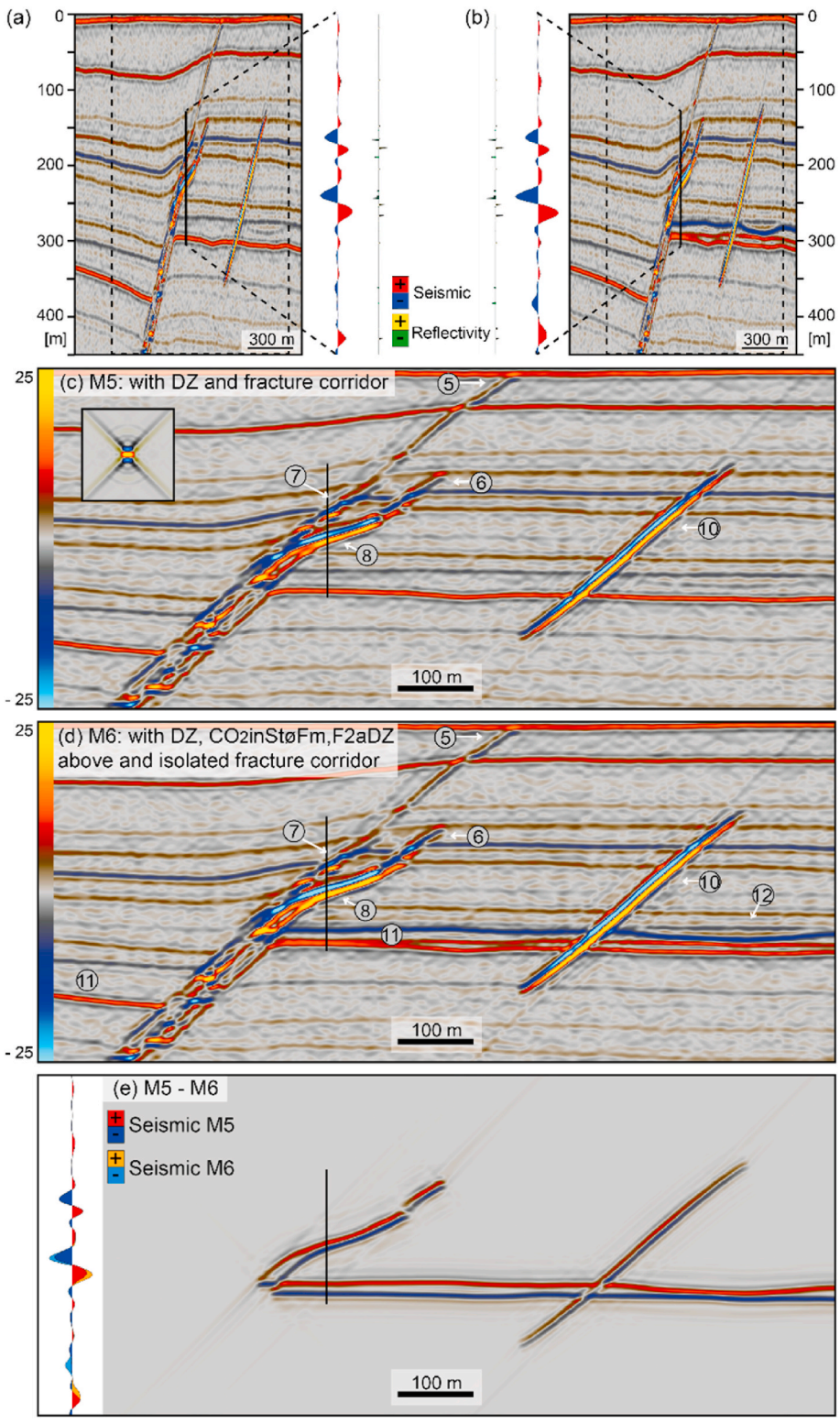

Fig. 9. Synthetic seismic sections with vertical exaggeration (VE) 5 of (a) M5: fault model with damage zone (DZ) and an isolated fracture corridor away from the fault and (b) M6: with damage zone and CO_2 filled in the thick sandstone layer in the footwall, in the fractures in the damage zone above this layer (in the footwall) and in the fracture corridor. The reflectivity (reflection coefficients) and corresponding synthetic wiggle trace for the interval marked with a vertical line shown for each model. Synthetic seismic section at 1:1 scale of (c) M5 and (d) M6 (location stippled square in a and b). The numbered labels point out key observations described in the text. (e) Difference plot of the synthetic seismic section of M5 (c) – M6 (d), and superposition of the seismic wiggle trace of M5 and M6. Abbreviations: Fm - Formation.

with damage zone and CO_2 in both the hanging wall and footwall (M3; Figs. 7c and 8c) shows less disturbance in the fault block between F2a and F2b than the model with damage zone and water-filled fractures (M2; Figs. 7b and 8b), but less internal layers than the model without damage zone (M1; Figs. 7a and 8a). The upper part of F2b has opposite polarity of the reflections (trough/peak) in M3 compared to M2 and M4, which, in the upper part are similar since the fractures in M4 are filled with gas only in the footwall of F2a (between #9/7 and #5 in Fig. 8b–d).

Fig. 8 also displays reflectivity and seismic wiggle traces for each model in a key location crossing the F2a and F2b and down to the thick sandstone layer (Figs. 3, 5 and 7). Closely spaced events in the reflectivity log compared to the seismic wiggle trace show widespread evidence of interference. Below the dotted line, the trace are the same for models M1-M5, and above the dotted line the wiggles for each model differs from each other. Where the CO_2 is present, the amplitudes are stronger (Figs. 8 and 9).

At a first glance, the models with damage zones (models M2-M6; Figs. 7–9) appear very similar, however, the difference plots and the superposed seismic wiggle traces for the comparisons between two and two models document differences (Figs. 9e and 10). Since M2-M4 have the same fault geometry, the changes in seismic response are related to the effect of CO_2 (Figs. 8 and 10), and the same is the case for M5 and M6 (Fig. 9e). In the difference plot between M3 and M4, there are two places along the fault zone where they are similar; hence no signal in the difference plots (Fig. 10c). This is where the thickest sandstone layers are present (Fig. 3b), which have no CO_2 within the damage zone as they contain no fractures. The effect of injecting CO_2 in the undamaged sandstone, the isolated fracture corridor and in the footwall damage zone above the sandstone layer is clearly visible in the difference plot of M5 and M6 (Fig. 9e).

4.3. Sensitivity analysis of key geophysical parameters

The effects of utilizing different wavelets and incident angles for M2 and M5 are shown in Fig. 11. The synthetic seismic sections emphasize the importance of resolution in conventional and high-resolution seismic datasets; there is more interference of the reflections in the conventional synthetic section (7 reflections in the interval of 90–200 m, compared to 14 in the same interval for the high-resolution, Fig. 11). In the conventional synthetic seismic the faulted block in between F2a and F2b is not resolved but is indicated by a disturbance (#13, Fig. 11b,d). Further, F2a and F2b are less prominent in the shallow part (above the faults splay around 240 m), but they can barely be detected at the termination near top layer 3 and at top of layer 8 (#5 and #6 in Fig. 11b, d).

The damage zone is not that well imaged in the conventional synthetic seismic sections compared to the high-resolution synthetic section, although it is possible to detect and identify the presence of the structure (#8, Fig. 11). The maximum width of the fracture corridor (5 m) is near the detection threshold for high-resolution data, and below the threshold for conventional seismic data. Despite this, the fracture corridor in M5 is imaged in both the high-resolution and conventional synthetic seismic section (Fig. 11c and d), with the fracture corridor seen as smeared reflections contrasting the surrounding reflective horizons

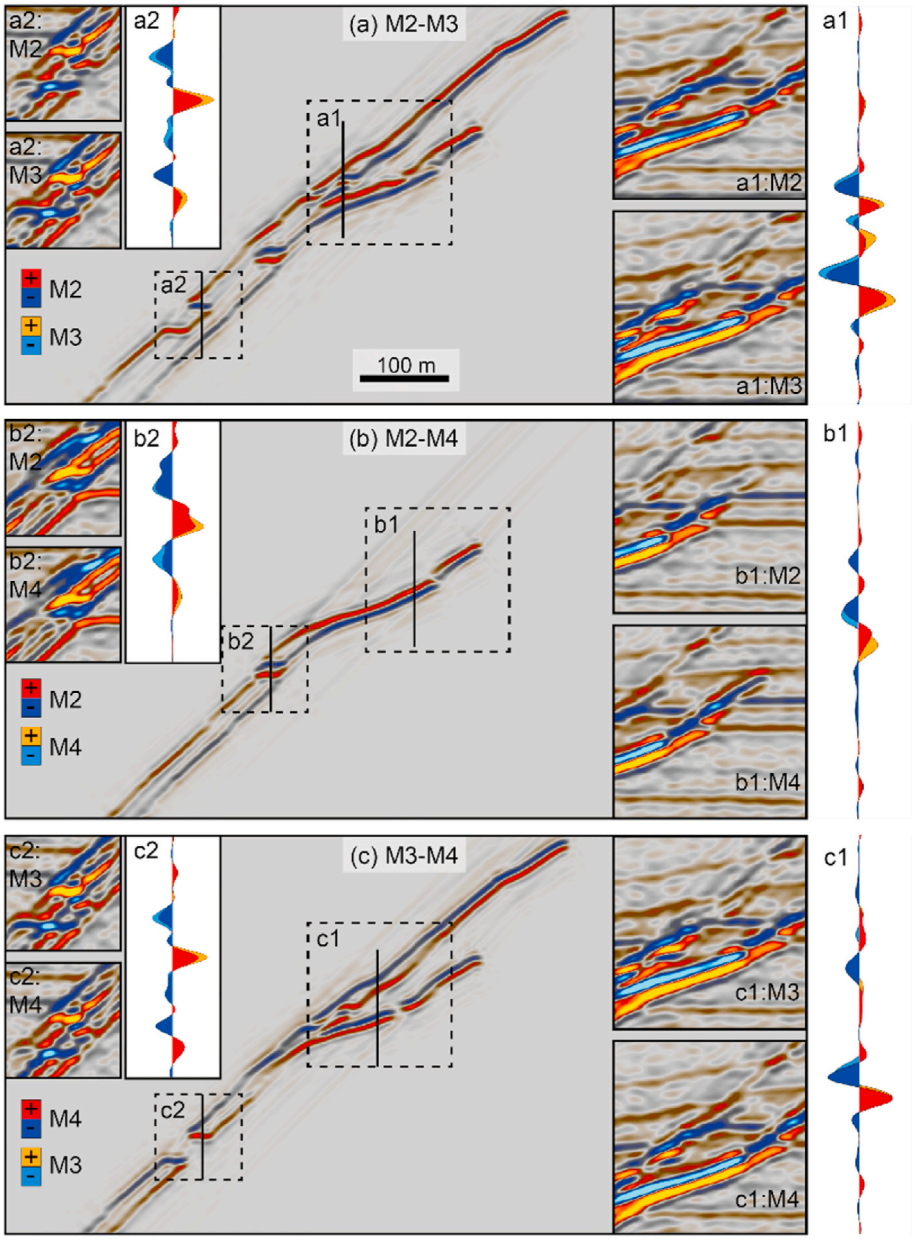

Fig. 10. Difference plots of models M2-M4. (a) M2 – M3, (b) M2 – M4 and (c) M3 – M4. All models have the same fault architecture, but different content in the damage zones (with and without CO_2). Each comparison include a difference plot and specific areas (marked as boxes on the difference plot) where also the synthetic seismic for each model is presented. In addition, superimposed seismic wiggle traces for the models are marked with a black line inside each box and shown on the side of the synthetic seismic.

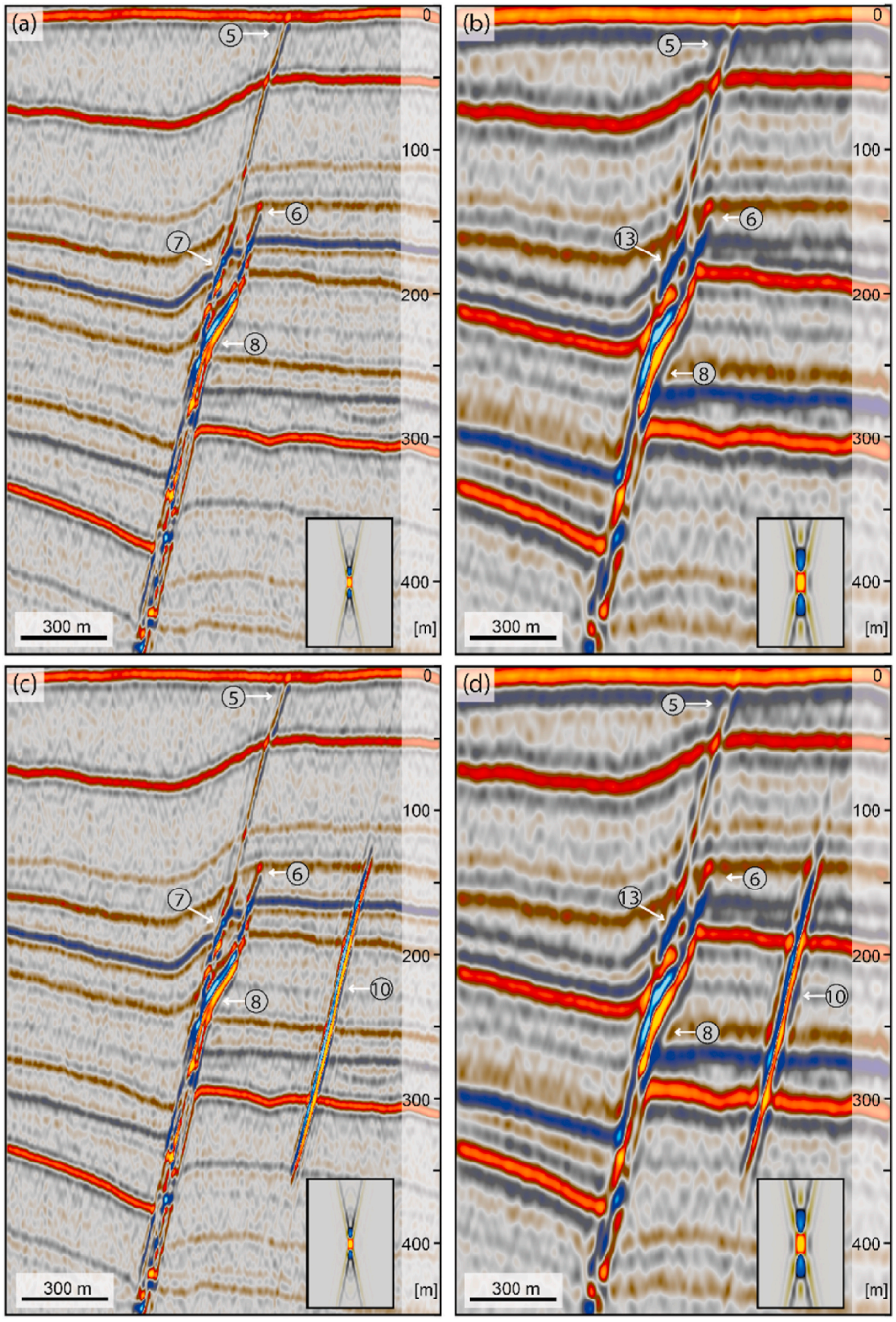

Fig. 11. Result of changing wavelet and incident angle corresponding to high-resolution seismic data (left) and conventional seismic data (right). High-resolution synthetic seismic section (a) and conventional synthetic seismic section (b) of the fault model M2 with damage zone. High-resolution synthetic seismic section (c) and conventional synthetic seismic section (d) of the fault model M5 with damage zone and an isolated fracture corridor away from the fault. Vertical exaggeration 5 for synthetic seismic and corresponding PSF.

(#10, Fig. 11).

The results of the sensitivity analysis of utilizing different illumination angles; 30°, 45° and 90° (perfect illumination) on M2 are shown in Fig. 12. For 45° and 90° illumination the fault is well imaged. However, the 30° illumination case has problems imaging most of the fault segments.

5. Discussion

Fault imaging in seismic data depends on geological constraints, such as truncation and offset of horizons, fault dip, geometry and intrinsic architecture, location of fault tips and process zones, and width and strain of relay ramps (3D aspects). The constraints combined with geophysical limitations (e.g., resolution) hinders fault interpretation. Most studies applying seismic modelling tools have targeted outcrop scenarios (e.g., Anell et al., 2016; Botter et al., 2017; Rabbel et al., 2018; Eide et al., 2018; Lubrano-Lavadera et al., 2018; Wrona et al., 2020). The advantage of using outcrops as conditioning is that they provide a viable geometric model (small details, geometries, segmentations etc.; Fig. 1). Shortcomings of this include the reliance on single unique locations often lacking measured petrophysical parameters. For some outcrops, samples are taken for laboratory petrophysical measurements but still there are uncertainties regarding how relevant these are making synthetic seismic for a subsurface cases. Another approach to building geological models for input to seismic modelling is by using analogue models (Kjoberg et al., 2017) or numerical discrete element models (DEM; Botter et al., 2014, 2016). This study is based on an approach that combines the impact of seismic and sub-seismic structures, such as damage zones, providing a realistic fault model, and has the potential to narrow the gap between seismic and outcrop data. Structural details

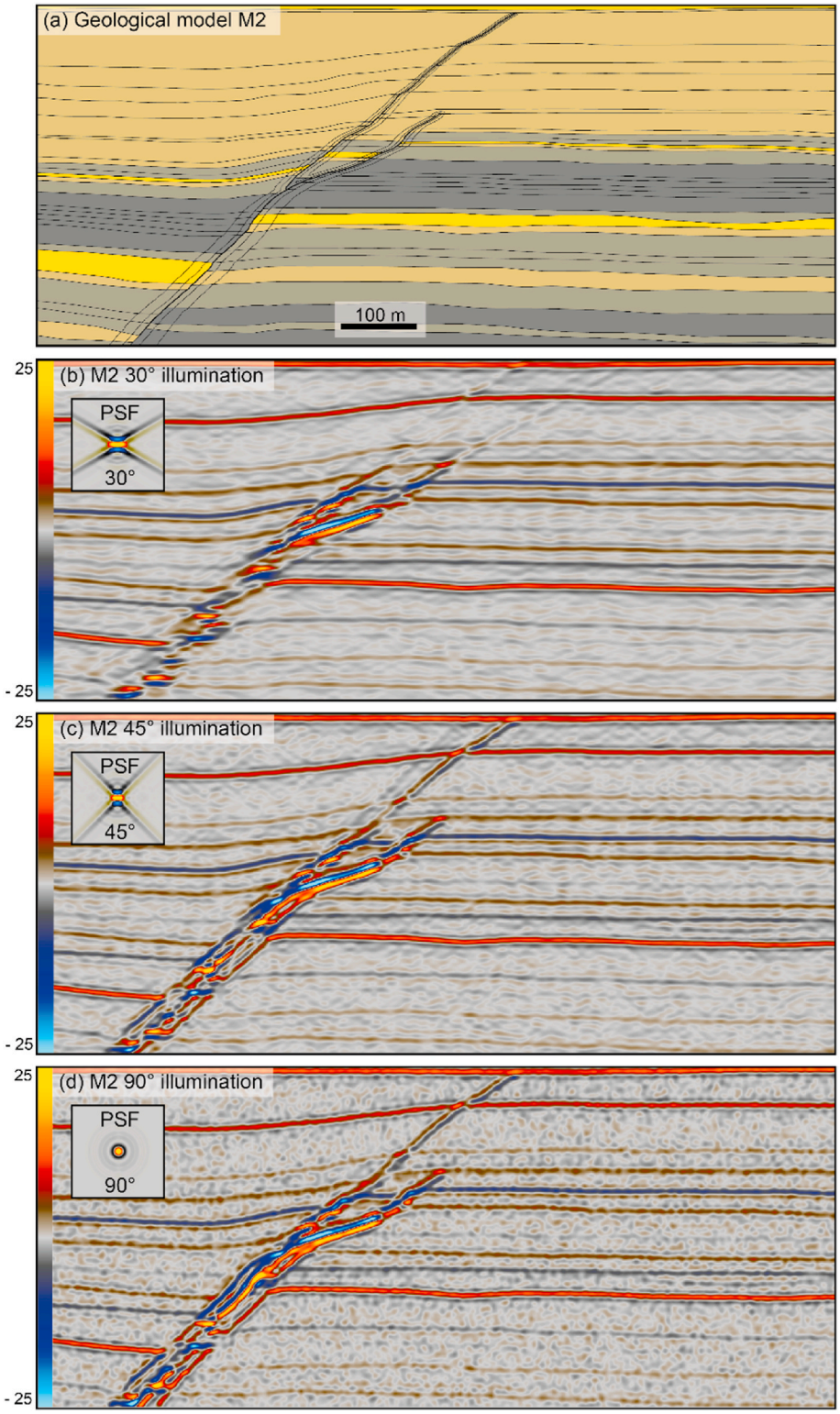

Fig. 12. (a) Geological model M2 in 1:1 scale. Colour scale as in Fig. 5. Result of changing illumination angle for M2 with (b) 30°, (c) 45° (as the rest of the synthetic seismic sections in the paper) and (d) 90° (perfect illumination). (For interpretation of the references to colour in this figure legend, the reader is referred to the Web version of this article.)

known from outcrop studies are combined with shallow subsurface geophysical and geological information based on high-resolution seismic data and well data. The Hoop area was selected because of its unique database for such a generic study addressing to what degree detailed fault architectures and gas seeps can be detected and resolved in seismic data.

5.1. Model building and conditioning

The model building in this study with conditioning of the two damage zone bins (inner and outer), with deformation bands and/or fractures for a combination of mixed lithologies, comes with uncertainties. These uncertainties can partly be ascribed to fault growth

mechanisms and rheology (Braathen et al., 2013) and partly to layer mechanics (Ogata et al., 2014; Ferrill et al., 2017). A model forecasting strict boundaries for deformation bands versus fracture damage zones, based in lithology and thereby excluding lithification effects (compaction, cementation), is a simplification. The forecasted changes in density and velocity for the inner and outer damage zone are therefore associated with uncertainties.

As the study is not directly based on outcrop data, where deformation features can be characterized in detail (e.g., types of deformation bands and fractures, frequency distribution etc.), simplifications to the models are made (Figs. 5 and 7). These simplifications are justified by the fact that seismic data resolution is below outcrop resolution, limiting what we can interpret from seismic data. The tuning of velocities for this study are literature based conceptual values (Sigernes, 2004; Botter, 2016; Botter et al., 2014, 2016; Agofack et al., 2018) and the density is estimated based on the estimated Vp. The succession was divided into four lithologies, and each layer is considered homogeneous for simplification (same velocity and density within each layer, differences inside and outside the damage zone; Fig. 5, Table 1 and Table A1 in Appendix A).

The basic fault model without a damage zone (M1; Figs. 3b and 7a) is based on high-resolution seismic data and hence represents an intermediate resolution case between outcrop and conventional seismic data (higher versus lower resolution, respectively). Design of the detailed models M2-M6 (Figs. 5 and 7) complies with the mentioned outcrop-derived empirical laws and gross geophysical conditioning. A natural next step would be to build and test fault models based on relevant outcrops having better resolution to make more detailed models to avoid the simplifications applied in this study. Ideally, this outcrop should also be sampled for laboratory measurements of key petrophysical parameters.

5.2. Seismic resolution and imaging of detailed fault architecture

Conventional 3D seismic data represent the norm for detailed fault studies in seismic data, while high-resolution P-Cable data still remains rare. The better resolution in the latter, however, allows greater recognition of details, such as subtle fault geometry and architecture. In this study, the P-Cable data achieves 3–7 m vertical resolution, compared to 15–25 m for the conventional seismic data. Structures at or below seismic resolution are clearly detected in the synthetic seismic (e.g., Figs. 8, 9 and 11). The introduction of gas within fractures of the damage zone (Figs. 8 and 10) and in a separate fracture corridor (Fig. 9), enhances the seismic signature of these features even further. These features are clearly detected in the synthetic seismic sections and show that tuning occurs within the limit of visibility (detection) and limit of separability (vertical resolution) in both types of seismic data (Fig. 11). In the high-resolution data, many of the details are resolved.

The fault models based on high-resolution seismic data from the Barents Sea provide a unique opportunity to investigate the use of high-resolution P-Cable data and the application of seismic attributes on both seismic data types for improving our capabilities in fault interpretation and gas detection. One limiting factor is that P-Cable data work best above the first seabed multiple in marine seismic data, hence covering the shallow subsurface (Planke et al., 2010; Lebedeva-Ivanova et al., 2018). In the study area, water depths are about 450 m (600 ms TWT), allowing high-resolution data down to 1200 ms TWT (about 900 m below the seabed). As the targeted faults, analysed herein are shallow (upper 500 m below the seabed; Fig. 3), attenuation of seismic energy with depth is limited (Brown, 2011). Also, changes in velocities within the studied depth interval appear moderate (2,2–3,2 km/s; Table A1 in Appendix A), limiting the impact of burial related compaction on velocity (Bjørlykke and Jahren, 2015). There is, however, a decrease in dominant frequency down to the targeted geology, from 150 Hz to 90 Hz for the high-resolution data, while the conventional data shows minimal changes.

The introduced fault architecture adds sub-seismic structures (deformation bands and fractures) that will ultimately affect the seismic image. Strikingly, these added structures show up in the synthetic seismic sections, and are enhanced when introducing gas within fractures of the damage zones and in the fracture corridor (Figs. 8–10). Resolution, and hence identification of fault damage zones, is sensitive to velocity. According to Boadu (1997), fracture-induced velocity changes become insensitive to fracture density at higher strains. This sensitivity reflects a shift to domineering fracture properties overshadowing rock properties.

When comparing seismic data to actual geology, it is important to consider the structural geometry in 1:1-scale so that the fault interpretation can be directly compared to faults in outcrop. Seismic sections are indeed often displayed with a high vertical exaggeration, which actually masks the impact of lateral resolution issues, though it is known that lateral resolution (combined with lack of illumination) are worse than the vertical resolution by at least a factor 2. In this study, most of the synthetic seismic sections are displayed in 1:1 scale (e.g., Figs. 8–10 and 12).

Seismic attributes do not change or improve the objective uncertainty. However, they can be applied in various combinations to highlight details not immediately apparent. The time-slices through the variance cube show signal discontinuities up to 60–80 m wide that could reflect faults with damage zones (Fig. 2c). Given the bin size of the high-resolution seismic data, and the corresponding horizontal resolution, these zones have been sampled up to ten times across the fault zone. The results are promising with respect to mapping the widths of damage zones at different depths in the subsurface for deformed sedimentary units, similar to the conclusions drawn by Alaei and Torabi (2017) from a study of conventional seismic data. Of concern is that both the results of this study, along with those of Alaei and Torabi (2017), yield conceivable damage zones that are wider than those predicted by outcrop-based global trend lines. A strength of the seismic data is the 3D control that we usually lack in outcrops.

The fracture corridor in the synthetic seismic sections appears similar to features discernible in the shallow subsurface seismic data of the Fingerdjupet Subbasin (Serck et al., 2017) and the Hoop graben (Fig. 13). When interpreting the subsurface seismic data (both areas are covered by conventional 3D seismic data with 2 ms processing), these features are overlooked as no obvious explanation is available; they are not minor faults as they lack evidence of throw. Notably, they appear strikingly similar to fracture corridors encountered in the synthetic seismic sections, suggesting they represent tabular zones of joints. As they appear in shale-dominated successions, there could be a link to compaction that triggers polygonal faulting.

5.3. Detection of gas

Faults are often associated with the formation of structural traps, and structural traps can be potential sites for CO_2 storage. The lithology, juxtaposition, damage zone and fault-core will determine if a fault zone will be sealing or act as a potential conduit for fluids (e.g., Ogata et al., 2014). Seismic modelling of CO_2 migration within a fault zone can provide insight into the detectability and seismic expression associated with such a scenario. This study focused on the detection of shallow CO_2 in a gaseous phase, different from the more higher density supercritical state in which CO_2 would be injected in a deeper reservoir. This study indicates that CO_2 within fault damage zones and fracture corridors creates a significant signal compared to the base case scenario (Figs. 9e and 10) suggesting that it will be possible to monitor and detect CO_2 leakage over time at repository locations.

A powerful tool for comparison and detection of differences in synthetic seismic sections is the application of difference plots, comparing two images that can identify subtle changes in signals. In our analyses, difference plots especially detect alterations between fault zones with a damage zone with and without CO_2 (Figs. 9e and 10).

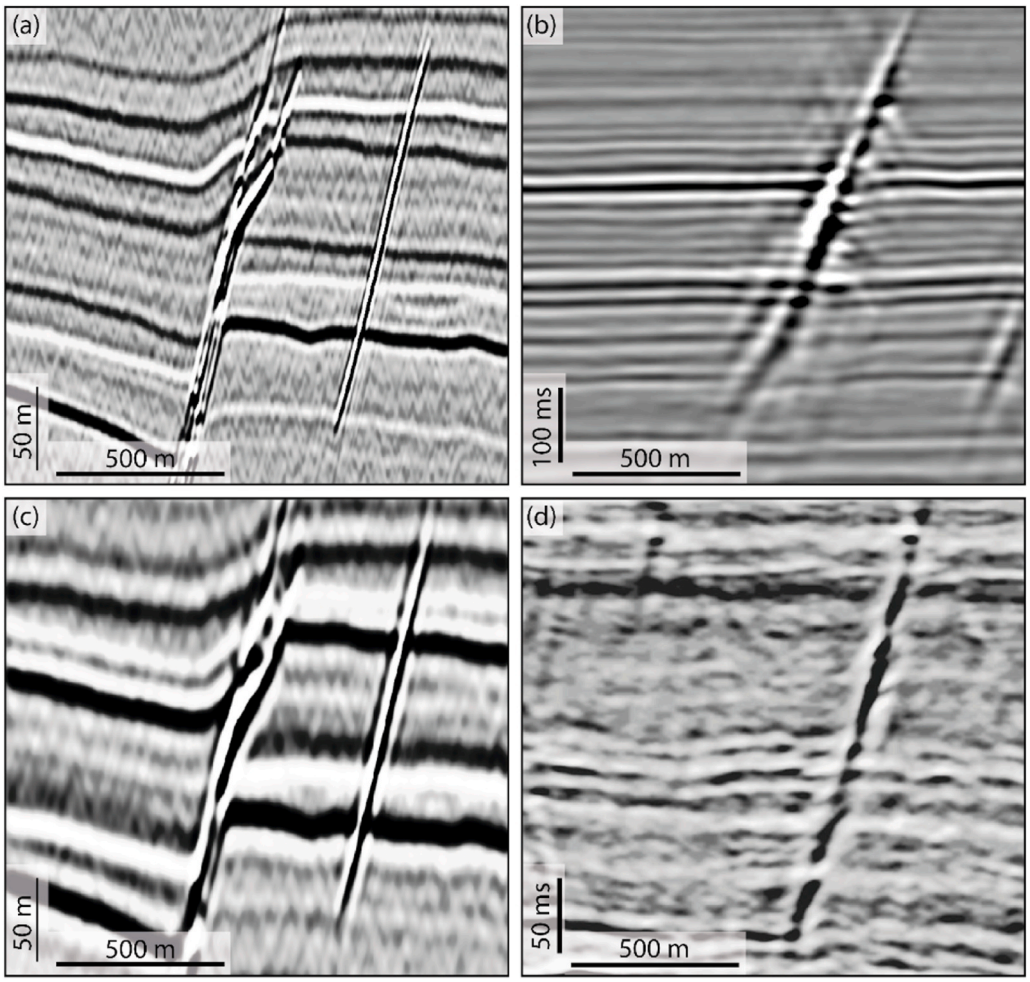

Fig. 13. (a) High-resolution synthetic seismic section of M5, same as in Fig. 9a. (b) Example of a possible fracture corridor in the Fingerdjupet Subbasin (pers comm. Christopher Serck, 2021; picture is mirrored). (c) Conventional synthetic seismic section of M5, same as in Fig. 11d. (d) Example of a possible fracture corridor in the Hoop Graben. Notice that the synthetic seismic data is in depth and actual seismic data in time.

Monitoring technologies rely on time-lapse comparative seismic to detect changes with time (Arts et al., 2003; Chadwick et al., 2004; Eiken et al., 2011; Furre and Eiken, 2014), much like the difference plots generated here (Figs. 9e and 10). A recent analysis by Waage et al. (2021) suggests P-Cable technologies can serve as a valuable monitoring tool in detecting even small (low percentage saturation) leakages at 30–300 times the detection limit of conventional seismic data. Further study into the limits in detecting different saturation models, with variations in distribution and changes in seismic parameters, would better constrain the threshold for identifying CO_2 migration.

6. Summary and conclusions

This study explores detection and resolution thresholds in synthetic seismic data on fault architecture and gas seeps associated with a shallow fault imaged in P-Cable, high-resolution seismic data. The results are based on a detailed geological model with viable fault architecture including sub-seismic structures of damage zones, which is conditioned by outcrop-based empirical laws for fracture and deformation band distribution. Elastic parameters are conditioned by strain in four lithologies; sandstone, shaley sandstone, sandy shale and shale; in which damage zones of sandstone layers host deformation bands contrary to shale layers with fractures, or a combination of the two. This study utilized a 2D PSF-based seismic convolution modelling to generate PSDM-alike synthetic seismic data, thus including full resolution and illumination effects, though in 2D only due to the input models.

The main findings of this study can be summarized as follows: (1) Adding damage zones to the baseline fault model gives rise to stronger disturbances of the seismic signals within a broader zone; (2) High-resolution seismic data have the ability to detect and outline damage zones in the shallow subsurface; (3) An isolated, narrow fracture corridor is clearly visible as dipping reflections crossing the horizons, which shows no stratigraphic offset; (4) CO_2-filled fractures in the damage zone and in the fracture corridor give a stronger seismic response than models without CO_2; (5) Sensitivity tests show good imaging for illumination $\geq 45^{\circ}$, which is the average dip of the main fault segment; (6) These findings offer guidance for seismic monitoring, e.g., building realistic models for seismic modelling simulating time-lapse (4D) seismic in relation to CO_2 storage.

Declaration of competing interest

The authors declare that they have no known competing financial interests or personal relationships that could have appeared to influence the work reported in this paper.

Acknowledgements

TGS, WGP and VBPR are greatly acknowledged for providing seismic data. This article is dedicated to COTEC and the NCCS-centre through grants by the Research Council of Norway (295061 and 257579). We thank Johannes Aglen Krakowski for discussion about model building

and conditioning, Jan Inge Faleide for discussions and Thorbjørn Dahlgren (Equinor) for providing important time/depth relation for the Gemini North well. We thank Schlumberger for academic license for Petrel software, NORSAR for academic license for SeisRoX and PETEX for MOVE software available at the University of Oslo. Charlotte Botter and two anonymous reviewers are thanked for thorough and constructive reviews.

Appendix

Table A1
Elastic parameters for the geological models.

	Base model without damage zone			Model including damage zone without CO2						Model including damage zone and CO2					
				Inner damage zone			Outer Damage zone			Inner damage zone			Outer Damage zone		
Layer/Block	Vp	Vs	Density	Vp	Vs	Density	Vp	Vs	Density	Vp	Vs	Density	Vp	Vs	Density
1	1.649	0.824	1.98												
2	1.905	0.907	2.04	2.073	0.751	2.03	1.973	0.717	2.07	1.934	0.744	2.02	1.722	0.730	2.00
3	2.121	0.769	2.10	2.333	0.845	2.15	2.227	0.807	2.13	2.030	0.837	2.08	1.938	0.799	2.06
4	2.454	0.889	2.16	2.699	0.978	2.23	2.576	0.933	2.21	2.348	0.968	2.16	2.241	0.924	2.13
5	2.426	0.878	2.21	2.668	0.966	2.23	2.547	0.922	2.20	2.321	0.956	2.15	2.216	0.913	2.13
6	2.424	0.967	2.22	2.666	1.064	2.23	2.545	1.017	2.20	2.320	1.075	2.15	2.214	1.026	2.13
7	2.642	1.056	2.26	2.907	1.256	2.28	2.774	1.200	2.25	2.529	1.224	2.20	2.414	1.168	2.17
8	2.824	1.132	2.30	3.106	1.245	2.31	2.965	1.189	2.29	2.703	1.233	2.24	2.580	1.177	2.21
9	2.877	1.274	2.23	3.165	1.445	2.33	3.021	1.379	2.30	2.753	1.431	2.25	2.628	1.365	2.22
10	2.787	1.230	2.01	3.043	1.362	2.30	2.905	1.300	2.28	2.648	1.349	2.22	2.527	1.287	2.20
11	2.677	1.200	2.30	2.961	1.068	2.31	2.405	1.146	2.27	1.853	1.077	2.04	2.056	1.157	2.30
12	2.590	1.162	2.28	2.864	1.217	2.29	2.322	1.294	2.25	1.736	1.204	2.02	2.020	1.271	2.08
13	2.587	1.358	2.23	3.363	2.507	2.36	2.975	2.227	2.29	3.363	2.507	2.36	2.975	2.227	2.29
14	2.587	1.345	2.28	2.845	1.480	2.26	2.718	1.412	2.24	2.475	1.445	2.13	2.363	1.378	2.16
15	2.673	1.256	2.24	2.298	1.131	2.16	2.006	1.103	2.21	1.919	1.115	2.01	2.249	1.162	2.13
16	2.307	1.272	2.26	1.744	0.931	2.00	2.325	1.091	2.15	1.517	0.882	1.93	2.023	1.071	2.08
17	2.035	1.394	2.26	1.701	0.969	1.99	2.268	1.177	2.14	1.480	0.959	1.92	1.973	1.165	2.07
18	2.775	1.278	2.31	1.665	0.894	1.98	2.220	1.086	2.13	1.449	0.885	1.91	1.931	1.075	2.06
19	2.600	1.198	2.50	1.595	0.830	1.95	2.086	1.008	2.10	1.361	0.822	1.88	1.815	0.998	2.02
20	2.604	1.130	2.49	1.562	0.781	1.96	2.083	0.960	2.09	1.359	0.783	1.88	1.812	0.951	2.02
21	2.788	1.395	2.53	1.673	0.970	1.98	2.231	1.177	2.13	1.459	0.992	1.91	1.941	1.165	2.09
22	2.930	1.612	2.37	2.152	1.631	2.11	2.421	1.721	2.17	1.672	1.614	2.04	2.106	1.704	2.10
23	2.709	1.820	2.25	3.022	2.368	2.19	2.116	2.092	2.12	3.022	2.368	2.19	2.116	2.092	2.12
24	2.673	1.646	2.12	2.741	1.910	2.28	2.807	1.728	2.26	2.508	1.752	2.20	2.442	1.711	2.18
25	3.106	1.581	2.55	2.485	1.423	2.18	2.720	1.522	2.25	2.162	1.403	2.11	2.432	1.497	2.18
26	3.106	1.590	2.56	2.494	1.431	2.18	2.795	1.510	2.25	2.167	1.417	2.11	2.431	1.495	2.18
27	3.193	1.693	2.43	2.595	1.632	2.20	2.874	1.722	2.27	2.223	1.615	2.13	2.500	1.705	2.19
28	3.127	1.734	2.42	3.439	1.573	2.37	3.203	1.683	2.35	2.952	1.953	2.29	2.898	1.864	2.27
29	2.984	1.761	2.48	2.387	1.585	2.11	2.686	1.673	2.23	2.077	1.569	2.08	2.036	1.656	2.16
30	3.075	1.712	2.51	1.945	1.199	2.03	2.490	1.456	2.18	1.505	1.187	1.90	2.160	1.441	2.15
31	3.250	1.936	2.44	2.606	1.606	2.21	2.926	1.695	2.28	2.262	1.598	2.16	2.545	1.678	2.20
32	3.342	1.795	2.51	2.905	1.249	2.07	2.674	1.517	2.23	1.745	1.237	2.00	2.326	1.592	2.15

References

Agofack, N., Lozovyi, S., Bauer, A., 2018. Effect of CO2 on P- and S-wave velocities at seismic and ultrasonic frequencies. Int. J. Greenh. Gas Control 78, 388–399. https://doi.org/10.1016/j.ijggc.2018.09.010. September.

Alaei, B., Torabi, A., 2017. Seismic imaging of fault damaged zone and its scaling relation with displacement. Interpretation 5 (4), SP83–SP93. https://doi.org/10.1190/int-2016-0230.1.

Anell, I., Lecomte, I., Braathen, A., Buckley, S.J., 2016. Synthetic seismic illumination of small-scale growth faults, paralic deposits and low-angle clinoforms: a case study of the Triassic successions on Edgeøya, NW Barents Shelf. Mar. Petrol. Geol. 77, 625–639. https://doi.org/10.1016/j.marpetgeo.2016.07.005.

Arts, R., Eiken, O., Chadwick, A., Zweigel, P., Van der Meer, L., Zinszner, B., 2003. Monitoring of CO2 injected at Sleipner using time lapse seismic data. In: Greenhouse Gas Control Technologies-6th International Conference. Pergamon, pp. 347–352.

Bastesen, E., Braathen, A., Skar, T., 2013. Comparison of scaling relationships of extensional fault cores in tight carbonate and porous sandstone reservoirs. Petrol. Geosci. 19 (4), 385–398. https://doi.org/10.1144/petgeo2011-020.

Berg, S.S., Skar, T., 2005. Controls on damage zone asymmetry of a normal fault zone: outcrop analyses of a segment of the Moab fault, SE Utah. J. Struct. Geol. 27 (10), 1803–1822. https://doi.org/10.1016/j.jsg.2005.04.012.

Bjørlykke, K., Jahren, J., 2015. Sandstones and sandstone reservoirs. In: Bjørlykke, K. (Ed.), Petroleum Geoscience: from Sedimentary Environments to Rock Physics. Springer Berlin Heidelberg, Berlin, Heidelberg, pp. 119–149. https://doi.org/10.1007/978-3-642-34132-8_4.

Boadu, F.K., 1997. Fractured rock mass characterization parameters and seismic properties: analytical studies. J. Appl. Geophys. 37 (1), 1–19. https://doi.org/10.1016/S0926-9851(97)00008-6.

Bond, C.E., 2015. Uncertainty in structural interpretation: lessons to be learnt. J. Struct. Geol. 74, 185–200. https://doi.org/10.1016/j.jsg.2015.03.003.

Botter, C., Cardozo, N., Hardy, S., Lecomte, I., Escalona, A., 2014. From mechanical modeling to seismic imaging of faults: a synthetic workflow to study the impact of faults on seismic. Mar. Petrol. Geol. 57, 187–207. https://doi.org/10.1016/j.marpetgeo.2014.05.013.

Botter, C., Cardozo, N., Hardy, S., Lecomte, I., Paton, G., Escalona, A., 2016. Seismic characterisation of fault damage in 3D using mechanical and seismic modelling. Mar. Petrol. Geol. 77, 973–990. https://doi.org/10.1016/j.marpetgeo.2016.08.002.

Botter, C.D., 2016. Seismic Imaging of Fault Zones: A Synthetic Workflow to Study the Impact of Faults on Seismic Images. University of Stavanger: Faculty of Science and Technology, Department of Petroleum Engineering. PhD thesis.

Botter, C., Cardozo, N., Qu, D., Tveranger, J., Kolyukhin, D., 2017. Seismic characterization of fault facies models. Interpretation 5 (4). https://doi.org/10.1190/INT-2016-0226.1. SP9–SP26.

Braathen, A., Osmundsen, P.T., Hauso, H., Semshaug, S., Fredman, N., Buckley, S.J., 2013. Fault-induced deformation in a poorly consolidated, siliciclastic growth basin: a study from the Devonian in Norway. Tectonophysics 586, 112–129. https://doi.org/10.1016/j.tecto.2012.11.008.

Braathen, A., Petrie, E., Nystuen, T., Sundal, A., Skurtveit, E., Zuchuat, V., Gutierrez, M., Midtkandal, I., 2020. Interaction of deformation bands and fractures during progressive strain in monocline - San Rafael Swell, Central Utah, USA: interaction of bands-fractures in monocline. J. Struct. Geol. 141 (June), 104219 https://doi.org/10.1016/j.jsg.2020.104219.

Braathen, A., Tveranger, J., Fossen, H., Skar, T., Cardozo, N., Semshaug, S.E., Bastesen, E., Sverdrup, E., 2009. Fault facies and its application to sandstone reservoirs. AAPG (Am. Assoc. Pet. Geol.) Bull. 93 (7), 891–917. https://doi.org/10.1306/03230908116.

Brown, A.R., 2011. Structural interpretation. In: Chapter 3 in Interpretation of Three-Dimensional Seismic Data, seventh ed., pp. 61–102. https://doi.org/10.1190/1.9781560802884.ch3.

Chadwick, R.A., Arts, R., Eiken, O., Kirby, G.A., Lindeberg, E., Zweigel, P., 2004. 4D seismic imaging of an injected CO2 plume at the Sleipner Field, central North Sea. In: Davies, R.J., Cartwright, J.A., Stewart, S.A., Lappin, M., Underhill, J.R. (Eds.), 3D Seismic Technology: Application to the Exploration of Sedimentary Basins, vol. 29. Geological Society of London, Memoir, pp. 311–320.

Childs, C., Manzocchi, T., Walsh, J.J., Bonson, C.G., Nicol, A., Schöpfer, M.P.J., 2009. A geometric model of fault zone and fault rock thickness variations. J. Struct. Geol. 31 (2), 117–127. https://doi.org/10.1016/j.jsg.2008.08.009.

Choi, J.H., Edwards, P., Ko, K., Kim, Y.S., 2016. Definition and classification of fault damage zones: a review and a new methodological approach. Earth Sci. Rev. 152, 70–87. https://doi.org/10.1016/j.earscirev.2015.11.006.

Cohen, K.M., Finney, S.C., Gibbard, P.L., Fan, J.X., 2013. The ICS international chronostratigraphic chart. Episodes 36, 199–204.

Eide, C.H., Schofield, N., Lecomte, I., Buckley, S.J., Howell, J.A., 2018. Seismic interpretation of sill complexes in sedimentary basins: implications for the sub-sill imaging problem. J. Geol. Soc. 175 (2), 193–209. https://doi.org/10.1144/jgs2017-096.

Eiken, O., Ringrose, P., Hermanrud, C., Nazarian, B., Torp, T.A., Høier, L., 2011. Lessons learned from 14 years of CCS operations: Sleipner. Salah and Snøhvit: Energy Proc. 4, 5541–5548. https://doi.org/10.1016/j.egypro.2011.02.541.EPNRCV1876-6102.

Faleide, T.S., Midtkandal, I., Planke, S., Corseri, R., Faleide, J.I., Serck, C.S., Nystuen, J. P., 2019. Characterisation and development of Early Cretaceous shelf platform deposition and faulting in the Hoop area, southwestern Barents Sea-constrained by high-resolution seismic data. Norw. J. Geol. 99, 1–20. https://doi.org/10.17850/njg99-3-7.

Faleide, T.S., Braathen, A., Lecomte, I., Mulrooney, M.J., Midtkandal, I., Bugge, A.J., Planke, S., 2021. Impacts of seismic resolution on fault interpretations: insights from seismic modelling. Tectonophysics 816, 229008. https://doi.org/10.1016/j.tecto.2021.229008.

Farazani, N., 2017. Reservoir Quality of the Stø Formation in the Hoop Fault Complex and Fingerdjupet Sub-basin, SW Barents Sea (The Transition between the Stø and Fuglen Formations). Master Thesis, UiO.

Ferrill, D.A., Morris, A.P., McGinnis, R.N., Smart, K.J., Wigginton, S.S., Hill, N.J., 2017. Mechanical stratigraphy and normal faulting. J. Struct. Geol. 94, 275–302. https://doi.org/10.1016/j.jsg.2016.11.010.

Fossen, H., Schultz, R.A., Shipton, Z.K., Mair, K., 2007. Deformation bands in sandstone: a review. J. Geol. Soc. 164, 755–769. Davis 1999.

Fossen, H., 2010. Structural Geology. Cambridge University Press, p. 463.

Fossen, H., Soliva, R., Ballas, G., Trzaskos, B., Cavalcante, C., Schultz, R.A., 2018. A review of deformation bands in reservoir sandstones: geometries, mechanisms and distribution. Geol. Soc. Spec. Publ. 459 (1), 9–33. https://doi.org/10.1144/SP459.4.

Furre, A.-K., Eiken, O., 2014. Dual sensor streamer technology used in Sleipner CO2 injection monitoring. Geophys. Prospect. 62, 1075–1088. https://doi.org/10.1111/1365-2478.12120.GPPRAR0016-8025.

Gabrielsen, R.H., Braathen, A., 2014. Models of fracture lineaments - joint swarms, fracture corridors and faults in crystalline rocks, and their genetic relations. Tectonophysics 628, 26–44. https://doi.org/10.1016/j.tecto.2014.04.022.

Gardner, G.H.F., Gardner, L.W., Gregory, A.R., 1974. Formation velocity and density-the diagnostic basics for stratigraphic traps. Geophysics 39, 770–780.

Kjoberg, S., Schmiedel, T., Planke, S., Svensen, H.H., Millett, J.M., Jerram, D.A., Galland, O., Lecomte, I., Schofield, N., Haug, Ø.T., Helsem, A., 2017. 3D structure and formation of hydrothermal vent complexes at the Paleocene-Eocene transition, the Møre Basin, mid-Norwegian margin. Interpretation 5 (3). https://doi.org/10.1190/INT-2016-0159.1. SK65–SK81.

Klausen, T.G., Müller, R., Sláma, J., Olaussen, S., Rismyhr, B., Helland-Hansen, W., 2018. Depositional history of a condensed shallow marine reservoir succession: stratigraphy and detrital zircon geochronology of the Jurassic Stø Formation, Barents Sea. J. Geol. Soc. 175 (1), 130–145.

Lebedeva-Ivanova, N., Polteau, S., Bellwald, B., Planke, S., Berndt, C., Stokke, H.H., 2018. Toward one-meter resolution in 3D seismic. Lead. Edge 37 (11), 818–828. https://doi.org/10.1190/tle37110818.1.

Lecomte, I., 2008. Resolution and illumination analyses in PSDM: a ray-based approach. Lead. Edge 27, 650–663. https://doi.org/10.1190/1.2919584.

Lecomte, I., Lavadera, P.L., Anell, I., Buckley, S.J., Schmid, D.W., Heeremans, M., 2015. Ray-based seismic modeling of geologic models: understanding and analyzing seismic images efficiently. Interpretation 3 (4), SAC71–SAC89. https://doi.org/10.1190/INT-2015-0061.1.

Lecomte, I., Lavadera, P.L., Botter, C., Anell, I., Buckley, S.J., Eide, C.H., Grippa, A., Mascolo, V., Kjoberg, S., 2016. 2(3)D convolution modelling of complex geological targets beyond – 1D convolution. First Break 34 (5), 99–107.

Lubrano-Lavadera, P., Senger, K., Lecomte, I., Mulrooney, M.J., Kühn, D., 2018. Seismic modelling of metre-scale normal faults at a reservoir-cap rock interface in Central Spitsbergen, Svalbard: implications for CO2 storage. Norw. J. Geol. 99 (2), 329–347. https://doi.org/10.17850/njg003.

Mendoza, J.S., Martinez, H.M.D., Stueland, E., 2019. Facies Characterization and Depositional Architecture of the Fruholmen and Stø Formation, Barents Sea, Norway. 2019. AAPG Annual Convention and Exhibition, San Antonio, Texas.

Michie, E.A.H., Mulrooney, M.J., Braathen, A., 2021. fault interpretation uncertainties using seismic data, and the effects on fault seal analysis: a case study from the horda platform, with implications for CO2 storage. Solid Earth Discuss. https://doi.org/10.5194/se-2021-23 [preprint].

Mondol, N.H., 2015. Well logging: principles, applications and uncertainties. In: Bjørlykke, K. (Ed.), Petroleum Geoscience: from Sedimentary Environments to Rock Physics, Second. Springer Berlin Heidelberg, pp. 385–425. https://doi.org/10.1007/978-3-642-34132-8_16.

Ogata, K., Senger, K., Braathen, A., Tveranger, J., 2014. Fracture corridors as seal-bypass systems in siliciclastic reservoir-cap rock successions: field-based insights from the Jurassic Entrada Formation (SE Utah, USA). J. Struct. Geol. 66, 162–187. https://doi.org/10.1016/j.jsg.2014.05.005.

Ottesen, D., Rise, L., Sletten Andersen, E., Bugge, T., Eidvin, T., 2009. Geological evolution of the Norwegian continental shelf between 61° N and 68° N during the last 3 million years. Norwegian Journal of Geology/Norsk Geologisk Forening 89 (4).

Planke, S., Berndt, C., Mienert, J., Bünz, S., Eriksen, F.~N., Eriksen, O.~K., 2010. P-cable: new high-resolution 3D seismic acquisition technology. In: EGU General Assembly Conference Abstracts, 12, 13618. May 2014.

Planke, S., Erikson, F.N., Berndt, C., Mienert, J., Masson, D., 2009. P-cable high-resolution seismic. Oceanography 22 (1). https://doi.org/10.5670/oceanog.2009.09, 85–85.

Rabbel, O., Galland, O., Mair, K., Lecomte, I., Senger, K., Spacapan, J.B., Manceda, R., 2018. From field analogues to realistic seismic modelling: a case study of an oil-producing andesitic sill complex in the Neuquén Basin, Argentina. J. Geol. Soc. 175 (4), 580–593. https://doi.org/10.1144/jgs2017-116.

Schueller, S., Braathen, A., Fossen, H., Tveranger, J., 2013. Spatial distribution of deformation bands in damage zones of extensional faults in porous sandstones: statistical analysis of field data. J. Struct. Geol. 52 (1), 148–162. https://doi.org/10.1016/j.jsg.2013.03.013.

Schaaf, A., Bond, C.E., 2019. Quantification of uncertainty in 3-D seismic interpretation: implications for deterministic and stochastic geomodeling and machine learning. Solid Earth 10 (4), 1049–1061. https://doi.org/10.5194/se-10-1049-2019.

Serck, C.S., Faleide, J.I., Braathen, A., Kjølhamar, B., Escalona, A., 2017. Jurassic to early cretaceous basin configuration(s) in the Fingerdjupet Subbasin, SW Barents Sea. Mar. Petrol. Geol. 86, 874–891. https://doi.org/10.1016/j.marpetgeo.2017.06.044.

Shuey, R.T., 1985. Simplification of the Zoeppritz equations. Geophysics 50 (4), 609–614. https://doi.org/10.1190/1.1441936.

Sigernes, L.T., 2004. Rock Physics of Extensional Faults and Their Seismic Imaging Properties, p. 366. Dissertation, PhD.

Torabi, A., Ellingsen, T.S.S., Johannessen, M.U., Alaei, B., Rotevatn, A., Chiarella, D., 2020. Fault zone architecture and its scaling laws: where does the damage zone start and stop? Geol. Soc. Lond. Spec. Publ. 496 (1), 99–124. https://doi.org/10.1144/sp496-2018-151.

Waage, M., Singhroha, S., Bünz, S., Planke, S., Waghorn, K.A., Bellwald, B., 2021. Feasibility of using the P-Cable high-resolution 3D seismic system in detecting and monitoring CO2 leakage. Int. J. Greenh. Gas Control 106, 103240.

Wibberley, C.A.J., Yielding, G., Di Toro, G., 2008. Recent Advances in the Understanding of Fault Zone Internal Structure: A Review, vol. 299. Geological Society Special Publication, pp. 5–33. https://doi.org/10.1144/SP299.2.

Worsley, D., 2008. The post-Caledonian development of Svalbard and the western Barents Sea. Polar Res. 27 (3), 298–317. https://doi.org/10.1111/j.1751-8369.2008.00085.x.

Wrona, T., Fossen, H., Lecomte, I., Eide, C.H., Gawthorpe, R.L., 2020. Seismic expression of shear zones: insights from 2-D point-spread-function based convolution modelling. J. Struct. Geol. 140, 104121 https://doi.org/10.1016/j.jsg.2020.104121. June.